Revised for *American Mineralogist*. **REVISION 1**

# Ferrian saponite from the Santa Monica Mountains (California, USA, Earth): Characterization as an analog for clay minerals on Mars with application to Yellowknife Bay in Gale Crater

A.H. Treiman[1], R.V. Morris[2], D.G. Agresti[3], T. G. Graff[4], C.N. Achilles[5,6], E.B. Rampe[2], T.F. Bristow[7], D.W. Ming[2], D.F. Blake[7], D.T. Vaniman[8], D.L. Bish[6], S.J. Chipera[9], S.M. Morrison[10], and R.T. Downs[10]

[1] Lunar and Planetary Institute, 3600 Bay Area Boulevard, Houston, TX 77058
[2] ARES Directorate, NASA Johnson Space Center, Houston TX 77058
[3] Department of Physics, University of Alabama at Birmingham, Birmingham, Alabama 35294-1170
[4] Jacobs Engineering, Houston, Texas 77058
[5] ESCG/UTC Aerospace Systems, Houston, TX, 77058
[6] Dept. of Geological Sciences, Indiana University, 1001 East Tenth St., Bloomington, IN 47405
[7] Exobiology Branch, NASA Ames Research Center, Moffett Field, CA 94035-1000,
[8] Planetary Science Institute, 1700 E. Fort Lowell, Tucson, AZ 85719-2395
[9] Chesapeake Energy Corporation, 6100 N. Western Ave., Oklahoma City, OK 73118
[10] Department of Geosciences, University of Arizona, Tucson AZ 85721

## Abstract

Ferrian saponite from the eastern Santa Monica Mountain, near Griffith Park (Los Angeles, CA), was investigated as a mineralogical analog to smectites discovered on Mars by the CheMin X-ray diffraction instrument onboard the Mars Science Laboratory (MSL) rover. The martian clay minerals occur in sediment of basaltic composition and have 02$\ell$ diffraction bands peaking at 4.59 Å, consistent with tri-octahedral smectites. The Griffith saponite occurs in basalts as pseudomorphs after olivine and mesostasis glass and as fillings of vesicles and cracks and has 02$\ell$ diffraction bands at that same position. We obtained chemical compositions (by electron microprobe), X-ray diffraction patterns with a lab version of the CheMin instrument, Mössbauer spectra, and visible and near-IR reflectance (VNIR) spectra on several samples from that locality. The Griffith saponite is magnesian, Mg/(Mg+ΣFe) = 65-70%, lacks tetrahedral $Fe^{3+}$ and octahedral $Al^{3+}$, and has $Fe^{3+}$/ΣFe from 64 to 93%. Its chemical composition is consistent with a fully tri-octahedral smectite, but the abundance of $Fe^{3+}$ gives a nominal excess charge of +1 to +2 per formula unit. The excess charge is likely compensated by substitution of $O^{2-}$ for $OH^-$, causing distortion of octahedral sites as inferred from Mössbauer spectra. We hypothesize that the Griffith saponite was initially deposited with all its iron as $Fe^{2+}$ and was oxidized later. X-ray diffraction shows a sharp 001 peak at 15Å, 00$\ell$ peaks, and a 02$\ell$ diffraction band at the same position (4.59 Å) and shape as those of the martian samples, indicating that the martian saponite is not fully oxidized. VNIR spectra of the Griffith saponite show distinct absorptions at 1.40, 1.90, 2.30-2.32, and 2.40 μm, arising from $H_2O$ and hydroxyl groups in various settings. The position of the ~2.31 μm spectral feature varies systematically with the redox state of the octahedrally coordinated Fe. This correlation may permit surface oxidation state to be inferred (in some cases) from VNIR spectra of Mars obtained from orbit, and, in any case, ferrian saponite is a viable assignment for spectral detections in the range 2.30-2.32 μm.

# Introduction

## Rationale from Mars Science Laboratory

The core objective of the Mars Science Laboratory (MSL) spacecraft mission as implemented by the rover *Curiosity* is to seek evidence of past habitable environments on Mars (Grotzinger et al., 2014). Pre-mission analyses of the Gale Crater landing site from martian orbit indicated a range of sedimentary rock deposits, of proper nature and age, that might either have been deposited in potentially habitable environments, or have transported rocks from such environments (Anderson and Bell, 2010; Milliken et al., 2010; Schwenzer et al., 2012; Wray, 2013). *Curiosity* landed a few hundred meters west of a local depression in which layered and fractured rocks were visible from orbit. The science team and engineering project management decided that the rocks of the depression were an attractive science target and would allow testing and verification of engineering operations, most notably drilling a rock, sieving the drill cuttings, and delivery of them to the CheMin ('Chemistry and Mineralogy') and SAM ('Sample Analysis at Mars') instruments. *Curiosity* traversed to the depression, informally named Yellowknife Bay, and documented the presence of sandstones and mudstones and several types of diagenetic (post-depositional) alterations that could reasonably have involved water.

In Yellowknife Bay, the *Curiosity* rover drilled twice into a mudstone, the Sheepbed stratum, in sites named John_Klein and Cumberland. The John_Klein site was chosen as typical of the Sheepbed exposures and contained white-colored crosscutting veinlets. The Cumberland site was chosen for its abundance of concretionary-like structures that were relatively resistant to weathering (Grotzinger et al., 2014). Clay minerals, signs of formation or alteration in aqueous environments, are present in both drilled samples (Fig. 1), a result established by the CheMin instrument from X-ray diffraction analysis (Vaniman et al., 2014) and confirmed by the SAM instrument by analysis of evolved gases released as a function of temperature (Ming et al., 2014).

The finding of clay minerals has huge importance for the goals of the MSL mission, but (of course) the analytical instruments on *Curiosity* allow only a small subset of the techniques that are commonly applied on Earth to characterize clay minerals and their geological contexts. Thus, we have sought terrestrial equivalents for the occurrences of clay minerals in the Sheepbed unit. This work is a detailed characterization of one possible terrestrial equivalent, the best

currently known with respect to results from CheMin, for the clay mineral detected by MSL at Gale Crater on Mars.

## Mineralogy of the Sheepbed Unit

As described by Vaniman et al. (2014), drilled rock fines from the John_Klein and Cumberland sites were sieved, and the <0.150 mm size fraction delivered to the CheMin instrument (Anderson et al., 2012), which produced 2-dimensional X-ray diffraction patterns of the materials (Blake et al., 2012). These patterns were converted to 1-dimensional patterns (Fig. 1a), and interpreted as to mineral identities and proportions using commercial software and reference diffraction patterns taken with laboratory equivalents of CheMin. Both rocks consist mostly of minerals characteristic of basalt: pyroxenes, plagioclase, and olivine, with minor alkali feldspar, pyrrhotite and Fe-Ti oxides. They also contain amorphous material (Morris et al., 2013) and minerals characteristic of low-temperature aqueous alteration, including smectite, Ca sulfate, hematite, and akaganeite, as well as abundant magnetite/maghemite interpreted as authigenic (Vaniman et al., 2014).

The presence of smectite minerals in the John_Klein and Cumberland samples is shown by the broad 001 diffractions at ~10.0 and 13.2 Å (Fig. 1a). However, the 001 diffraction is not characteristic, by itself, of exact clay mineral species because its position varies according to the speciation of the interlayer cations and their hydration state. Many standard methods for characterizing clay minerals by XRD (e.g., glycolation and cation exchange) cannot be performed by the MSL payload and, furthermore, the 2θ range of the MSL CheMin instrument (~5 to 50° 2θ, CoKα) does not include the position of the 06$\ell$ diffraction band, which is normally used to differentiate between di-octahedral and tri-octahedral smectites. Instead, Vaniman et al. (2014) used the position of the 02$\ell$ diffraction band to make this distinction. They report that its position for both John_Klein and Cumberland (22.5° 2θ, CoKα; 4.59 Å d-spacing) implies a tri-octahedral smectite because the maximum in the 02$\ell$ diffraction bands are at lower 2θ (greater d-spacing) than reference di-octahedral smectites and more similar to reference tri-octahedral smectites, although still at somewhat lower 2θ (Vaniman et al., 2014). This small difference between the martian smectites and the reference tri-octahedral smectites results from the speciation of the cations in the octahedral sites of martian versus terrestrial reference smectites.

Here, we report on the X-ray, chemical, and spectroscopic properties of saponite from Griffith Park CA as an analog to the Sheepbed smectites. The Griffith Park material was specifically selected for this study because it has an 02$\ell$ diffraction band similar in location and shape to those of the Sheepbed smectites (Vaniman et al., 2014), it is an iron-bearing tri-octahedral smectite, and sufficient quantities are available for future studies (commercially, from museums, and from field collection). The Griffith Park saponite, originally reported by Larsen and Steiger (1917), has been studied extensively for applications in materials science and catalysis (Larsen and Steiger, 1928; Rodriguez et al., 1994, 1995; Vicente-Rodrigues et al., 1996; Vicente et al., 1996, 1997, 1998; Komadel et al., 2000; Komadel, 2003; Gandia et al., 2005; Komadel and Madejova, 2006; Stuki, 2006). However, the geological setting of its formation and its properties relevant to Mars are poorly known. Our purpose here is to characterize Griffith saponite and its formation mechanisms for comparison with the smectite minerals detected by CheMin in Gale Crater, for comparison to clay minerals detected from martian orbit by visible and near-infrared (VNIR) spectroscopy, and for comparison to Mössbauer data obtained by the Mars Exploration Rovers.

## Saponite from Griffith Park: Description and Geologic Setting

Iron-bearing saponite was recognized first in Griffith Park, Los Angeles, CA, by Larsen and Steiger (1917) as fillings of amygdules (vesicles) in Miocene basalts of the Topanga Canyon Formation in the eastern Santa Monica mountains (Critelli and Ingersoll, 1995). The saponite was originally given the mineral name ‘griffithite,’ and identified as a chlorite species because of its appearance as black lustrous crystals, up to 0.5 mm across, with strong platy cleavage. This ‘griffithite’ loses significant water on heating to 55°C (Larsen and Steiger, 1928), consistent with it being a saponite, but was still classified as a chlorite (Neuerburg, 1951) until thermal and X-ray data confirmed that it was a smectite (Faust, 1955), specifically a mixed Mg-$Fe^{3+}$-$Fe^{2+}$ tri-octahedral smectite (Komadel, 2003). The mineral name ‘griffithite’ was then discredited (Fleischer, 1955), but is occasionally used as a varietal name (e.g., Pecuil, 1996; Vicente et al., 1996; Changela and Bridges, 2011). Here, we will call this material Griffith saponite to distinguish it from smectites and saponite from other localities.

The type locality for the Griffith saponite is Griffith Park, City of Los Angeles, California. The exact location may no longer be available, as it was at the southern end of

Cahuenga pass in an area now covered by the Hollywood Freeway, Cahuenga Boulevard, and the Hollywood Bowl (Larsen and Steiger, 1917; Neuerburg, 1951). The type locality is in the lower member of the Topanga Canyon Formation, of Miocene age, which is a complex sequence of marine arkosic sediments, basaltic volcaniclastic sediments, basalts, and rare limestones (Neuerburg, 1953; Yerkes and Campbell, 1979; Critelli and Ingersoll, 1995). "Large sills and irregular intrusive bodies of dark brown basalt are common in the lower member of the Topanga Formation. Many of these intrusives are amygdaloidal; the distribution of the amygdules is erratic and appears to have no relation to contacts or to inclusions. Veins of zeolites and related minerals are common in these intrusive rocks. The texture ranges from porphyritic and intergranular to intergranular; most specimens of intrusive rock are porphyritic. Phenocrysts generally comprise about 10 percent to 15 percent of the rock; the minerals are andesine-labradorite, augite, and in some specimens olivine. The groundmass consists predominantly of andesine with a little augite and magnetite; chlorite [=smectite] and chlorophaeite (?) fill spaces in the groundmass" (Neuerburg, 1953).

Saponite is also found in rocks of the overlying middle member of the Topanga Canyon Formation. The middle member is a complex of basaltic volcaniclastic sediments, including mudstones, conglomerates, and sandstones (Neuerburg, 1953). "Small angular to sub rounded fragments of various types of basalt are set in a matrix of dark brown, opaque, claylike material that has a waxy luster (chlorophaeite?) [= saponite]. Mineral fragments consist of andesine, oligoclase, quartz, and augite, with minor amounts of myrmekite, analcite, biotite, and zircon. The boulders and cobbles consist primarily of augite basalt and olivine basalt with a few boulders and pebbles of pink granite, quartz diorite, quartzite, acidic porphyries, and arkose" (Neuerburg, 1953).

All of the basaltic rocks of the Topanga Canyon formation show effects of low-temperature aqueous alteration. In them, saponite is locally abundant, and zeolites of several species are locally common, as are other aqueous alteration phases including zoisite and prehnite (Neuerburg, 1951).

# Samples and Methods

## Samples

We examined saponite in three samples of altered basalt from the Griffith Park area, Los Angeles, CA (Fig. 2). We have neither exact localities nor geological settings for any of these samples, except the general data given in the Introduction. One sample was obtained from the American Museum of Natural History (AMNH 89172); another set of samples was purchased from Minerals Unlimited (MU); a third sample, purchased from M & W Minerals, had been in the collection of the California Academy of Sciences (CAS). The AMNH and CAS samples are old enough that they had been curated as distinct mineral species, and so likely came from the type locality (now under the Hollywood Bowl).

A mineral separate of saponite was prepared from each sample by manually disaggregating and handpicking a portion of the sample. For the AMNH and MU samples, saponite was extracted manually from filled vesicles. From the CAS sample, we prepared three separates from vesicle fill material: fine-grained brown clay, coarse black clay, and white spherules (see below in Petrography). Portions of the mineral separates were cut to form thick sections for electron microbeam imaging and elemental analysis and portions were dry ground and dry sieved to <0.150 mm for analysis, in sequence, by backscatter Mössbauer spectroscopy (MB), X-ray diffraction (XRD), visible, near IR reflectance spectroscopy. It is likely that each handpicked separate contains a few percent of other materials.

For comparison with the Griffith saponite samples, we also analyzed by XRD a number other smectites: API33A (Garfield nontronite), PHY07 (Pennsylvania nontronite), SWa-1 (ferruginous smectite), NAu-1 (Australian nontronite), and WASCDB1 (nontronite), SWy1 and BSDMNT1 (Na-montmorillonite) and SAz-1 and STx1 (Ca-montmorillonite). The samples were analyzed as the <0.150 mm size fraction except for PHY07, which was analyzed as the <0.038 mm size fraction.

## Methods

**Electron Microbeam.** Portions of the saponite -bearing samples were cut to form thick sections for electron microbeam imaging and elemental analysis. The section surfaces were smoothed with abrasives down to laps with 3 μm diamond powder embedded in plastic. It was not possible to polish these samples, as the soft saponite plucked out, leaving a rougher surface

than before polishing. Thus, the section surfaces are not optically flat as required for precise quantitation with EMP. In addition, the saponite -bearing samples changed significantly during the few minutes of vacuum before carbon coating. The saponite -rich areas changed from black to tan color and became visibly rougher. Thus, one cannot expect good quantification in the EMP analyses, and analytical totals are significantly less than 100% even for anhydrous minerals like pyroxene and plagioclase (Tables 1,2); of course, analyses of saponite have even lower totals because of their structural OH (Table 3). However, we believe that element abundance ratios are not affected significantly by surface roughness, see below in 'Results'.

Sections were imaged in backscattered electron (BSE) and secondary electron (SEI) modes and analyzed for element abundances using the CAMECA SX-100 electron microprobe at the Ares Directorate, Johnson Space Center, Houston TX. Analytical conditions were nominal for the instrument and laboratory. Peak intensities were measured for Kα radiation of these elements using these well-characterized standards: Si, diopside; Ti, rutile; Al, oligoclase; Cr, chromite; Fe, fayalite; Ni, NiO; Mn, rhodonite; Mg, diopside or forsterite; Ca, diopside; Na, oligoclase; K, orthoclase; and S, anhydrite. No significant quantities of S were detected, so S is not given in Table 3 The incident electron beam was at 15 kV and 10 nA, and defocused to 10 μm diameter on standards and samples. Peak X-ray intensities were counted for 30-60 seconds, and backgrounds were counted for the same total time. Analytical standards were run as unknowns to validate the calibrations, which were crosschecked against plagioclase and pyroxene adjacent to the smectite.

**Powder X-ray Diffraction.** Transmission X-ray diffraction patterns for Griffith saponite samples were acquired at room temperature using the CheMin IV instrument at the ARES Directorate, Johnson Space Center. CheMin IV is a laboratory version of the MSL CheMin flight instrument and is used to baseline its capabilities (Blake et al., 2012). The CheMin IV at ARES is configured with an $N_2$ gas (derived from liquid $N_2$) inlet tube so that measurements can be made in a dry $N_2$ atmosphere or in (humid) lab air. The CheMin IV, like MSL CheMin, acquires CoKα diffraction patterns in transmission geometry using radiation from powder samples that are continuously vibrated ultrasonically to agitate the material and achieve a variety of crystal orientations in the sample cell. The detector is energy sensitive, which permits post-analysis filtering to yield only diffracted (and scattered) CoKα X-rays and to exclude CoKβ X-rays and characteristic X-rays fluoresced from the target sample.

**Mössbauer Spectroscopy**. Backscatter Mössbauer (MB) spectra ($Fe^{57}$: 14.4 keV) were acquired at room temperature using MIMOS-II spectrometers from SPESI. The spectrometers are laboratory equivalents of the instruments onboard the Mars Exploration Rovers (Klingelhöfer et al., 2003) with additional radiation shielding and without a reference source. The instruments were oriented vertically, so that the γ-ray beam is pointed at the ceiling and powder samples were oriented horizontally on glassine paper substrates, which are essentially transparent to the 14.4 keV γ-rays. All measurements were made in laboratory air. The source radiation was $^{57}$Co(Rh) with spectra acquired in 512 channels (folded to 256 channels). MB velocity calibration was done using the spectrum for metallic Fe foil acquired at room temperature, the MIMOS-II differential signal spectrum, and the program *MERView* (Agresti et al., 2006). MB parameters (isomer or center shift (CS), quadrupole splitting (QS), hyperfine field strength ($B_{hf}$), and subspectral areas of Fe-bearing phases (A)) were obtained by a least squares fitting procedure with the program *MERFit* (Agresti et al., 2009).

**Reflectance Spectroscopy**. VNIR reflectance spectra between 0.35 and 2.5 μm were acquired at ~25 °C with Analytical Spectral Devices (ASD) FieldSpec3 spectrometers configured with ASD Mug Lights. One instrument was located to make measurements in (humid) lab air. A second instrument was located inside a one-atmosphere glove box configured with a transfer chamber (Plas-Lab); the glove box and transfer chamber interiors were independently and continuously purged with dry-$N_2$ gas derived from liquid $N_2$. Co-located in the glove box were a hot plate (Fisher Isotemp), a dewpoint meter (Vaisala DRYCAP DM70) to measure the $H_2O$ content, relative humidity (RH), and temperature of the dry $N_2$ atmosphere (100 – 180 ppmv, <0.5%, and ~25-30 °C, respectively), and an IR thermometer (Fluke Model 66) to measure hot plate and sample surface temperatures. Spectralon (SRS-99-010; Labsphere, Inc.) was used as the reflectance standard. The spectra from the three detectors in the ASD instrument were spliced using software supplied with the instrument.

VNIR spectra were obtained in lab air for all samples. Spectral measurements for saponite sample AMNH85172_PHY were also acquired during desiccation under dry $N_2$ at room temperature, 110°C, and 220°C for 436, 1152, and 212 hours, respectively. Note that these spectral measurements were all made at room temperature in the dry $N_2$ environment of the glove box; the cool-down time from 110 °C and 220 °C to ambient was a few minutes. The sample was remeasured in lab air after 16 hours exposure to that environment.

# Results

## Petrography

The Griffith saponite occurs in rocks of basaltic composition, both basalts proper and clastic sediments composed primarily of basaltic detritus. The basalts consist of saponite, augite, plagioclase, titanomagnetite, and ilmenite (Figs. 3a,e,g,h,i). The original textures of the basalts were sub-ophitic (augite partially enclosing plagioclase euhedra) to intersertal (glassy mesostasis among augite and plagioclase). From the compositions of the plagioclase and pyroxene (Figures 4a, b), notably the absence of low-Ca pyroxene, the basalts were likely not tholeiitic, i.e. they were alkali olivine basalts (Hoots, 1931). Relict olivine is reported is some basalts of the Topanga Canyon formation (Neuerberg, 1953), but our samples contained none.

Griffith saponite was originally recognized as filling vesicles (amygdales) in the Topanga Canyon Formation basalts (Larsen and Steiger, 1917; Neuerburg, 1951; Critelli and Ingersoll, 1995) and occurs as such in all three of our samples (Figs. 3c,d,e,f,h). In addition, saponite is also present in two other petrographic settings. Saponite replaces olivine in the basalts, both as phenocrysts and anhedral grains among pyroxene and plagioclase (Figs. 3b,d,i). In neither case are former olivine grains surrounded by expansion fractures, as are common when olivine is replaced by serpentine (O'Hanley, 1996). Finally, saponite occurs in areas that consisted of mesostasis material, among crystals of olivine, augite, and feldspar (Figs. 3a,e,i,j); this mesostasis was probably glass with quench crystals, including elongate laths of ilmenite, and dendritic, hollow grains of titanomagnetite (Figs. 3f,g,j). There is no evidence that plagioclase or augite were replaced by saponite.

The CAS sample shows evidence of several varieties of low-temperature or hydrothermal alteration, which are best exposed in the filled vesicles. Going from vesicle wall to center, the first alteration product is fine-grained tan-colored saponite material (possibly the 'chlorophaeite' of Neuerburg, 1951); this material is also present as crack-fillings. The fine-grained saponite has a conchoidal fracture, and shows no crystal shapes, cleavages, or faces (to <5 μm as apparent in secondary electron imagery). This material is denoted as 'Vf-f,' fine-grained vesicle fill, in Figures 1-3 and Table 3. Next inward in some vesicles is a white shell or sphere of silica, shown in X-ray diffraction to be α-quartz, i.e., agate or chalcedony (Fig. 2f, g), which is reported as veinlets near the type area for Griffith saponite (Neuerburg, 1953). The silica contains small

proportions of at least two other phases, an iron oxide and an unidentified Ca-Mg-Al silicate (Figs. 3f). Interior to both fine-grained saponite and silica (where present) is coarse-grained saponite, 'Vf-c' in Figure 2 and Table 3, in grain sizes up to ~100 μm (Fig. 2d). The coarse-grained saponite fills the cores of vesicles, and occasionally the cores of silica spherules. Similar coarse-grained saponite also replaces olivine phenocrysts and crystals in the basalts, commonly with the saponite (001) crystal planes perpendicular to crystallographically oriented cracks across the original olivine (Fig. 3b). Mesostasis areas among the plagioclase and pyroxene of the basalt are also replaced by material rich in saponite, but it is difficult to classify it as fine- or coarse-grained (Fig. 3 g,j).

The AMNH and MU samples contain only coarse-grained saponite as a common alteration material; no fine-grained saponite or silica was noted. In the AMNH and MU samples, coarse-grained saponite is present as vesicle fills, as replacements of olivine, and as replacements of mesostasis.

## Properties of Griffith Smectite

**Chemistry.** The chemical compositions and crystal chemistry of Griffith saponite (Table 3) are based on EMP chemical analyses and on Mössbauer spectroscopy for iron speciation and siting (Table 4). The EMP chemical analyses are of lower quality than would normally be acceptable for rock-forming minerals, in terms both of analytical totals and variability (Table 3). The low totals, averaging 85-91% wt. (Table 3), are caused by three factors: inherent $H_2O$/OH content, polish, and porosity. The saponites must retain structural OH, even through desiccation in high vacuum; ideally, dehydrated (not dehydroxylated) saponites like these should contain ~5% wt. $H_2O$ equivalent (e.g., Larsen and Steiger, 1917). Good EMP analyses rely on having an optically flat surface, and it was not possible to polish the saponite in our samples – it is soft and greasy, and plucked out on polishing so we could only flatten the surfaces to a grit size of 3 μm. Thus, this surface roughness affects analytical totals, even on the anhydrous phases like augite and plagioclase (Tables 1,2). Finally, the analyzed saponite was distinctly porous, as seen in secondary electron imagery (Fig. 3b,c). The porosity includes original intergranular space and porosity developed as the saponite dehydrated during sample preparation and analyses. For reference, the type Griffith saponite contained ~17% wt. $H_2O$ (Larsen and Steiger, 1917). The variability in chemical analyses derives partially from the roughness of the sample surfaces, and

the random orientations of those roughness elements with respect to X-ray detectors (and thus X-ray paths). In theory, the average of many analyses ought to even out this variability. Analyses of saponite in mesostasis areas are even more variable, because of relict unaltered phases. From the many analyses of mesostasis area, we have culled out those that clearly contain plagioclase feldspar, ilmenite, and/or titanomagnetite (Fig. 3g, j). However, it was not possible to distinguish small contributions from any of these phases from inherent variability of the saponite.

The chemical compositions of the Griffith saponite samples are generally similar, but with some significant differences. Among all the samples and textures, saponite shows limited variability in most cations; abundances of Al, Fe, and Mg are very similar (Table 3), and average Mg#s range only from 65% to 71% (Table 3). A puzzling difference among these samples is MnO abundance, which is an order of magnitude greater in the MU samples than in the AMNH and CAS samples. The greatest differences are in abundances of interlayer cations: Ca, Na, and K. The AMNH saponite, in all its textural settings, has significantly lower Ca than the MU and CAS samples, but an intermediate Na content.

The Griffith saponite analyzed here is similar to, but not identical with, analyses in the literature (Table 3; Fig. 5), showing that its chemical composition and Fe redox state are not narrowly fixed. The literature analyses tend to have higher Al and Si contents, slightly lower Mg#s, and $Mn/FeO_T$ ratios intermediate between MU and AMNH (and CAS). Our Griffith saponite samples include those with the lowest $MnO/FeO_T$ and lowest $Fe^{3+}/\Sigma Fe$ ratios analyzed to date, excluding Larsen and Steiger (1917) who report chemical and Fe redox data but no Mössbauer, XRD, or VNIR data. There is general agreement that Griffith saponite has ~17 wt.% equivalent $H_2O$ (Table 3). Our EMP analyses (in vacuum) show an average deficit of ~13 wt.% in good agreement with the value of 12.3 wt.% reported by Larsen and Steiger (1917) for non-hydroxyl $H_2O$. Comparisons of these analyses are clearer in the normalized formulae, which are discussed below.

**Iron Mineralogy and Redox State.** Results of Mössbauer spectroscopy (Table 4) constrain the speciation and siting of iron in the saponite -bearing samples. Mössbauer spectra of Griffith saponite samples have three or four doublets that are assigned to $Fe^{2+}$ and $Fe^{3+}$ in octahedral coordination (Fig. 6; Table 4; e.g. Gates et al., 2002; Cashion et al., 2008). Samples AMNH85172_PHY and MUGPLA1_PHY are characterized by two $Fe^{3+}$ doublets (doublet 3D1 with CS = 0.37 ± 0.02 mm/s and QS = 1.35 ± 0.02 mm/s and doublet 3D2 with CS= 0.38 ± 0.02

mm/s and QS = 0.80 ± 0.02 mm/s) and one $Fe^{2+}$ doublet (doublet 2D1 with CS = 1.14 ± 0.02 mm/s and QS = 2.62 ± 0.02 mm/s). Doublet 3D1 has an unusually high value of QS for $Fe^{3+}$, indicating that the anions coordinated to that $Fe^{3+}$ are quite assymetric, i.e. the coordination is highly distorted. The other two saponite samples (CASGP1-C and –F) have these three doublets plus one additional $Fe^{3+}$ doublet (3D3 with CS =0.32 ± 0.02 mm/s and QS =0.42 ± 0.02 mm/s). We assign this doublet to a nanophase ferric oxide (npOx) phase, which would include any combination of ferrihydrite, hisingerite, superparamagnetic hematite, and superparamagnetic goethite; none of these substances diffract coherently, and would not be apparent in XRD in the inferred proportions (Table 4). The Mössbauer spectra and parameters imply that the $Fe^{3+}$ is entirely in octahedral coordination. On the basis of XRD and other data, Kohyama et al. (1973) and Kohyama and Sudo (1975) consider that the weathering sequence (under oxidizing and humid conditions) is "ferrous iron rich saponite" (i.e., ferrosaponite) to "ferric iron-rich saponite" (i.e., ferrian saponite) to hisingerite.

Kohyama et al. (1973) also report Mössbauer data for iron-rich (and MgO-poor) saponite using a two-doublet fitting model (one doublet each for $Fe^{2+}$ and $Fe^{3+}$). For the ferrous doublet, they report CS ranges from 1.14 to 1.19 mm/s and QS ranges from 2.52 to 2.86 mm/s, with QS decreasing gradually with increasing extent of oxidation. For the ferric doublet, they report CS ~ 0.36 mm/s and QS ranges from 0.86 to 0.96 mm/s. These data are in good agreement with our measurements. For the ferrous doublet, the CS values are comparable and our value of QS (2.62 mm/s) is intermediate. For the ferric doublet, direct comparison is not possible as we used a two ferric-doublet fitting model. However, the values of CS are all comparable (and therefore insensitive to the fitting model), and the values of QS for the one-doublet fit are intermediate to those for the two-doublet fit (0.80 and 1.35 mm/s), a result expected using one-doublet versus two-doublet ferric fitting models. Considering the difference in fitting models and bulk composition (MgO-poor versus MgO-rich for Griffith saponite), the Mössbauer data are in good agreement.

We calculate the $Fe^{3+}/\Sigma Fe$ ratio for the Griffith saponite using doublets 3D1, 3D2, and 2D1. Our Griffith saponite samples have variable proportions of $Fe^{3+}$ and $Fe^{2+}$ in octahedral sites with $Fe^{3+}/\square Fe$ ranging from 0.64 for the most reduced sample (AMNH89172_PHY) to 0.85 – 0.92 for the most oxidized (CASGP1-C, CASGP1-F, and MUGPLA1_PHY).

Mössbauer, chemical, and other data for Griffith saponite are discussed by Vincente et al. (1998) and Komadel et al. (2000), although they do not report Mössbauer CS and QS values. Their samples have $Fe^{3+}/\Sigma Fe \sim 0.90$, which is equivalent to values for our samples originally sourced from the California Academy of Sciences (CASGP1-C and –F) and Minerals Unlimited (MUGPLA1_PHY). Comparison of MnO concentrations (Table 3) reveals that the Vincente et al. (1998) and Komadel et al. (2000) samples of Griffith saponite correspond to our MUGPLA1 sample. Perhaps not coincidentally, their samples were also obtained from Minerals Unlimited. The Griffith saponite analyzed by Larsen and Steiger (1917, 1928) is more like our AMNH sample with respect to $Fe^{3+}/\Sigma Fe$ (0.46) and MnO concentration (Tables 1 and 2; Fig. 5).

The fine-grained saponite sample (CASGP1-F) also shows a small sextet that is assigned to crystalline hematite (Table 4) and is presumably present as a matrix contamination; this sample also contains some quartz (Fig. 7). The Mössbauer spectrum of the basalt separate (AMNH89172_BAS) shows the saponite doublets (3D1, 3D2, and 2D1), an additional $Fe^{2+}$ doublet (2D2) presumably from pyroxene, a hematite sextet (S1), and the magnetite pair of sextets (S2A and S2B) (Table 4). The pyroxene and magnetite correspond to igneous pyroxene and titanomagnetite as discussed above (Fig. 3c,e).

**Crystal Chemistry.** The crystal chemistry of the Griffith saponite samples is given in the bottom half of Table 3. It is based on EMP chemical analyses, Mössbauer Fe speciation and site assignment, and the assumption of a normal 2:1 phyllosilicate formula: $I_{0\text{-}2}M_{4\text{-}6}T_8O_{20}(OH)_4 \cdot nH_2O$, where I, M and T refer respectively to cations in interlayer, octahedral (metal), and tetrahedral sites. Because the Griffith saponite contain insignificant ferric iron in tetrahedral coordination (as shown by the Mössbauer data), the analyses were normalized to Si+Al=8 to fill the tetrahedral sites. For these calculations, we assume that the $Fe^{3+}$ now present as npOx (CASGP1-C and –F) was originally integral to the saponite crystal structure, i.e. in the octahedral layer (Newman and Brown, 1987).

By crystal chemistry, our Griffith saponite samples are fully tri-octahedral, with 6 octahedral cations per 8 tetrahedral cations (Si+Al) within the 1σ uncertainties (Table 3). The octahedral sites are filled dominantly by Mg and Fe in a ratio near 2:1, with small or insignificant proportions of other cations. Formally, these clay minerals are (magnesian) saponites or, considering their abundance of $Fe^{3+}$, ferrian saponites. Their interlayer cation compositions are dominated by Ca, and are unremarkable.

The structural normalizations of Table 3 all have excess cation charge compared to a 'normal' saponite formula, $I_{0-2}M_{4-6}T_8O_{20}(OH)_4 \cdot nH_2O$. The AMNH and CAS samples have total apparent formula charges of ~ +1 (within 1σ uncertainties), while the MU samples have a total apparent formula charge of ~ +2. These apparent charge excesses are not artifacts of analysis, as they are greater than what might arise from analytical uncertainties (Table 3). The apparent excess charges must be balanced somehow, and two mechanisms seem possible: unanalyzed interlayer cations and deprotonation of structural OH. Additional interlayer cations, contributing 1 or 2 charges per formula unit (Table 3), could balance the excess charge in the analyzed formulae. Possible unanalyzed interlayer cations include Li, Sr, and/or Ba. However, we think deprotonation is a more likely explanation: that one or two of the structural $OH^-$ groups in the formula is replaced by $O^{2-}$. This is a known oxidation mechanism for phyllosilicates (Farmer et al., 1971; Borggaard et al., 1982; Lear and Stucki, 1985; Rancourt et al., 1993), and is consistent with the inferred distortion in the octahedral sites for the Mössbauer 3D1 doublet (above).

**X-ray Diffraction.** X-ray diffraction patterns for our Griffith saponite samples (Figure 7) are consistent with diffraction patterns in the literature (Vicente et al., 1996, 1997; Komadel et al., 2000). All the patterns show a strong 001 diffraction near 15 Å, a series of 00ℓ diffractions, and a distinct 02ℓ diffraction band near 4.6 Å. The strength and sharpness of the 00ℓ diffractions imply that the Griffith saponite is highly crystalline, with little layer disordering, intercalations, or interstratifications; this is consistent with the appearance of the saponite as glossy plates. Because of the sharpness of the 001 peak, the Lorentz-polarization correction (Reynolds, 1986; Moore and Reynolds, 1997) resulted in negligible change in position except for sample AMHN 89172_PHY equilibrated in dry $N_2$ in the CheMin-IV (11.8 Å versus 11.9 Å after the correction). The positions of the 00ℓ diffractions vary strongly and reversibly with hydration state (Fig. 8, Table 5). Griffith saponite (AMNH89172_PHY and CASGP1-C) dehydrated under dry $N_2$ gas collapses to an 001 spacing of ~12 Å, implying a change from ~2 layers of $H_2O$ interlayer to <1 (Bish et al., 2003). On heating to ~220°C in dry $N_2$, Griffith saponite (AMNH89172_PHY) collapses further to a 001 spacing of ~10 Å, i.e. nearly no interlayer water (spectrum not shown).

It is noteworthy that the intensities of the 004 and 005 diffractions of the Griffith saponite vary with hydration state (Fig. 8). For the dehydrated saponite, with no water or hydroxyl layer between adjacent T-O-T layer packages, the 004 diffraction (at ~3 Å) corresponds to the distance between adjacent layers of oxygens (or of cations) in that package. For the hydrated saponite, the

005 diffraction at ~3 Å corresponds again to the distance between adjacent layers of oxygens in the saponite if it contains a single layer of oxygens (water or hydroxyl) between the T-O-T layer packages.

The 02$\ell$ diffraction band is important as a measure of the unit cell 'b' dimension of the octahedral layer of the smectite structure, and thereby of the nature of the cations in the octahedral layer. Di-octahedral smectites have smaller 02$\ell$ distances (i.e. greater 2θ values) than do tri-octahedral smectites, as shown in Figure 9 by a comparison of the montmorillonite and nontronite 02$\ell$ bands with that of the tri-octahedral saponite SapCa-1. The Griffith saponite samples all have 02$\ell$ spacings significantly greater than any di-octahedral smectite, and even greater than the magnesian saponite SapCa-1 (Fig. 9). This comparison suggests that the Griffith smectite is tri-octahedral (Vaniman et al. 2014). The Griffith saponite samples analyzed here show a range for the maximum in the 02$\ell$ band, from a minimum near that of SapCa-1 at 4.55 Å to a maximum of 4.59 Å, and a positive correlation between the 02$\ell$ maximum (in degrees 2θ) and $Fe^{3+}/\Sigma Fe$. The positive correlation extrapolates to the ferrosaponite studied by Chukanov et al. (2003) (02$\ell$ = 4.72 Å and $Fe^{3+}/\Sigma Fe = 0.27$). That maximum 02$\ell$ value for Griffith (ferrian) saponite is identical to the one reported by Vaniman et al. (2014) for the smectites in the martian samples John Klein and Cumberland. If the correlation between 02$\ell$ maximum and oxidation state is valid, iron in the martian Sheepbed saponites is incompletely oxidized.

**VNIR Reflectance Spectroscopy**. Reflectance spectra for the four separates of Griffith saponite are shown in Figure 10a. All are characterized by overlapping $Fe^{2+}$ and $Fe^{3+}$ electronic and $Fe^{2+}$ -$Fe^{3+}$ charge transfer absorptions between ~0.35 μm and ~1.3 μm. Qualitatively, this region of the smectite VNIR spectrum resembles that for chlorite, which also has $Fe^{2+}$ and $Fe^{3+}$ (King and Clark, 1989). The reflectance of AMNH89172_PHY is considerably lower than those of the other three samples over this region (0.22 versus ~0.40 at 1.0 μm), presumably because it has the lowest $Fe^{3+}/\Sigma Fe$ ratio (Table 4). We have labeled the absorptions centered near 1.4, 1.9, and 2.1 to 2.5 μm as "OH", "HOH", and "MOH". Spectral features in the OH region result from stretching and stretching plus bending vibrations of the $H_2O$ molecule ($2\nu_1$, $2\nu_3$, $\nu_1+\nu_3$, $2\nu_2+\nu_1$, and $2\nu_2+\nu_3$, where $\nu_1$ and $\nu_3$ are the stretching fundamental vibrations and $\nu_2$ is bending fundamental vibration of the $H_2O$ molecule) and O-H stretching vibrations of the M-OH group (where M = $Fe^{2+}$, $Fe^{3+}$, and Mg in saponite, Table 3). Spectral features in the 1.9 μm region

result from a combination of $H_2O$ bending and stretching fundamental vibrations ($\nu_2+\nu_1$ and $\nu_2+\nu_3$). Note that if the $H_2O$ molecule is absent, spectral features near 1.9 μm will not be present. Spectral features in the MOH region result from combinations of the OH stretching and bending fundamentals of the MOH group. For tri-octahedral smectites, MOH spectral features are expected from cations in octahedral sites (normally $(Al,Mg,Fe^{2+},Fe^{3+})_3OH$), OH spectral features are expected from $(Al,Mg,Fe^{2+},Fe^{3+})_3OH$ and interlayer $H_2O$, and HOH spectral features are expected from interlayer $H_2O$. Adsorbed but not interlayer $H_2O$ would also contribute to OH and HOH spectral features.

The positions of the OH, HOH, and MOH spectral features for the Griffith saponite samples are compiled in Table 5. As expected for saponite equilibrated in lab air, and directly shown by the XRD data with 001 peaks at ~15 Å (Table 5), absorption features from interlayer water, near 1.4 and 1.9 μm, are prominent. Continuum-normalized spectra for the MOH region are plotted Figure 10b, and show two well-defined minima. The position of the more intense band is variable, ranging from 2.300 to 2.315 μm. The position of the less intense band ranges from 2.395 to 2.401 μm, and there is a shoulder at longer wavelengths indicating the presence of unresolved bands there.

The position of the ~2.31 μm spectral feature can be interpreted in terms of the redox state of the octahedrally coordinated $Fe^{2+}$ and $Fe^{3+}$. Referring to Table 5, the saponite (AMNH89172_PHY) with the lowest value of $Fe^{3+}/\Sigma Fe$ (=0.64) has the longest wavelength for the MOH band (2.315 μm). Conversely, the two saponites (CASGP1-C and –F) with the largest values of $Fe^{3+}/\Sigma Fe$ (0.89 and 0.90) have the shortest wavelengths for their MOH bands (2.300 and 2.301 μm). The MU saponite (MUGPLA1) has intermediate values of $Fe^{3+}/\Sigma Fe$ (0.85) and of MOH position (2.308 μm). This spectral analysis is consistent with various laboratory studies which report that the OH stretching vibration (2.6 to 2.9 μm region) shifts to longer wavelengths with possible concurrent formation of tri-octahedral domains upon chemical reduction of structural $Fe^{3+}$ in nontronite, a di-octahedral $Fe^{3+}$ smectite, and Griffith saponite to $Fe^{2+}$ (Stucki and Roth, 1976; Komadel et al., 1995, 2000; Manceau et al., 2000; Fialips et al. 2002; Komadel, 2003). Recently, Chemtob et al. (2014) report a shift to shorter wavelengths for the MOH spectral region upon oxidation of $Fe^{2+}$ to $Fe^{3+}$ in an iron rich, synthetic saponite.

Our crystal-chemical analysis of AMNH89172_PHY (Table 3) gives $Mg/(Fe^{2+}+Fe^{3+}) = 2$ for the octahedral sites. This ratio, plus the value of $Fe^{3+}/\Sigma Fe$ (0.64; Table 5), are consistent with

assignment of the MOH spectral feature at 2.315 μm to ($Mg_2Fe^{3+}_{0.64}Fe^{2+}_{0.36}$)-OH. Similarly, we can assign the 2.308 μm spectral feature for MUGPLA1B to ($Mg_2Fe^{3+}_{0.85}Fe^{2+}_{0.15}$)-OH. If we assume that the Mössbauer doublet 3D3 (Table 4) for samples CASGP1-C and –F is associated with saponite and not npOx, then the MOH band near 2.300 μm in those samples can be associated with ($Mg_2Fe^{3+}_{0.92}Fe^{2+}_{0.08}$)-OH.

As shown in Figure 11 for AMNH89172_PHY, desiccation greatly reduces the intensity of the spectral feature at ~1.9 μm, as interlayer $H_2O$ is removed (Fig. 11b), because that feature requires the presence of the $H_2O$ molecule. In comparison, the depth of the spectral features at 2.30 – 2.32 μm are relatively constant because they represent ($Mg,Fe^{2+},Fe^{3+}$)$_3$-OH and not interlayer $H_2O$. The positions of these two spectral features are also invariant with respect to desiccation. For the spectral feature near 1.4 μm, desiccation both reduces its intensity (from loss of interlayer $H_2O$) and changes its position from 1.413 to 1.404 μm (from enhanced contribution of hydroxyl bound to octahedrally coordinated cations relative to hydroxyl bound to H) (Fig. 11c). Note that changes in intensity of the OH and HOH spectral features are essentially reversible upon re-exposure of the sample to lab air.

**Conclusions.** The chemical and physical properties of the Griffith saponite samples are all similar, although there are some distinct differences. The chemical compositions of all Griffith samples examined are consistent with fully tri-octahedral saponite, with the octahedral sites completely filled (dominantly with Fe and Mg) and with no evidence for octahedral $Al^{3+}$ or tetrahedral $Fe^{3+}$. Most of the iron in Griffith saponite is $Fe^{3+}$, ranging from 64% of all iron to 93%. With so much ferric iron, the nominal formula for a saponite does not charge-balance, with an overall excess charge of +1 to +2, well outside of nominal uncertainties. This apparent charge excess is likely compensated by substitution of $OH^-$ in the typical saponite structure by $O^{2-}$ – a common mechanism for iron oxidation in phyllosilicates. This suggests that iron in the original saponite was likely all (or mostly) ferrous, and that the current range of $Fe^{3+}$ abundances arose by later oxidation. Interlayer cations in Griffith saponite are dominated by Ca. The VNIR spectra are typical for smectite minerals, and the position of the absorption near 2.3 μm varies with the Fe oxidation state.

## Formation of the Griffith Smectite

Chemical and textural evidence suggests that the saponite in Griffith Park samples was

deposited from aqueous solution associated with dissolution of olivine and glass from the host basalts. The saponite forms pseudomorphs after olivine (Fig. 3c), with the saponite (001) cleavages oriented perpendicular to void spaces occurring as crystallographically oriented cracks in the olivine crystal (Fig. 3b). This observation suggests that orientations of the saponite crystals were controlled by that of the host olivine (Eggleton, 1984; Delvigne, 1998, p. 129; Wilson, 2004). Saponite pseudomorphs after olivine are not surrounded by expansion cracks (Fig. 3b,f,j), suggesting that replacement of olivine by saponite was isovolumetric. Because saponite contains substantial $H_2O$ and olivine does not, the replacement could not have been isochemical – a significant proportion of Mg, Fe, and Si from the olivine must have been removed into solution. Similarly, the chemistry of the saponite also shows that it did not form isochemically: saponite replacing olivine contains substantial Al, which must have come from outside the olivine, perhaps from the mesostasis glass. And, saponite replacing mesostasis glass contains substantial Mg, which would not have been abundant in the mesostasis; perhaps the Mg came from the olivine. In fact, the saponite has essentially the same composition throughout a sample, independent of its physical setting, which implies that all were deposited from an aqueous solution that allowed free chemical exchange across each rock. The mass lost from replacement of olivine and mesostasis with saponite may have been deposited in vesicles and cracks as more saponite.

It is puzzling that the CAS sample contains smectite in two textural varieties, coarse- and fine-grained, with essentially the same composition (Table 3) and separated in some areas by a quartz deposit. If this sequence of deposits represents three events or episodes of aqueous alteration, then the two varieties of smectite likely would have different chemical compositions, which they do not (Table 3). A possible solution to this difficulty is if the coarse-grained smectite was deposited from fluid into void spaces (as in the AMNH and MU samples), but that the fine-grained smectite replaced a pre-existing material that lined vesicles and cracks. It is possible, though perhaps impossible to prove, that the pre-existing material was glass from late-stage magma, mobilized within the cooling basalt to fill cracks and line vesicles. After this material solidified, quartz was deposited from solution to partially fill vesicles. Only then was the rock extensively altered to form smectite, both as deposits from solution and as replacements of olivine and glass.

Mössbauer spectroscopy shows that most of the iron in the tri-octahedral Griffith saponite

samples is $Fe^{3+}$. Most $Fe^{3+}$-rich and Mg-poor smectites are di-octahedral and fall in the montmorillonite-nontronite series [i.e., $I_{0-2}(Al^{3+},Fe^{3+})_4T_8O_{20}(OH)_4 \cdot nH_2O$]. Thus, it seems likely that the iron in the Griffith saponite was not $Fe^{3+}$ as originally deposited, but was $Fe^{2+}$ and was subsequently oxidized. This inference is consistent with evidence that ferroan saponites oxidize rapidly in nature and in laboratory settings under atmospheric $O_2$ (e.g., Badaut et al. 1985; Chuckanov et al., 2003; Neuman et al. 2011; Chemtob et al., 2014).

## Other Occurrences

The formation of the Griffith saponite, as a low-temperature alteration product of basalt (and other mafic rock), is typical for iron-bearing saponite on Earth and elsewhere: "Ferromagnesian tri-octahedral smectites (saponite / iron saponite series) … are widespread in nature, especially as the main authigenic clay mineral produced by the alteration of oceanic and continental basalts and other basic volcanic material" (Güven, 1988). The textural settings of the Griffith saponite are also typical for altered basalts, e.g. "…Fe-rich smectites are the dominant alteration products, occurring either as pseudomorphs or infilling veins and vesicles" (Walters and Ineson, 1983). Among the many other reports of basaltic material altered to ferroan saponite or ferrosaponite, one can cite: Kodama et al. (1988), April and Keller (1992), Robert and Goffé (1993), Köster et al. (1999), Parsatharathy et al. (2003), Mas et al. (2008), and Haggerty and Newsom (2013). Ferromagnesian tri-octahedral smectite is also found in deep-sea deposits (Bischoff, 1972; Scheidegger and Stakes, 1977; Badaut et al., 1985; Parra et al., 1985), which are, in a broad sense, also related to the alteration of basalts.

Ferromagnesian smectites are known in some martian rocks, specifically the nakhlite martian meteorites (Treiman, 2005). The nakhlites contain ferromagnesian smectites that formed, on Mars, by aqueous alteration of olivine, siderite, and silicic glass (Treiman et al., 1993; Treiman, 2005; Changela and Bridges, 2011). The bulk chemical compositions of these alteration products are more ferroan and less aluminous than in Griffith saponite, and they do not normalize well into the formula for smectite: for Si+Al=8, the sum of nominally octahedral cations far exceeds the limit of 6 for a tri-octahedral smectite. This discrepancy could suggest that the nakhlite saponites contain significant Mg in their interlayers, in addition to in their octahedral sites.

Ferromagnesian smectites are also found in other planetary settings, most notably in

chondritic meteorites and interplanetary dust particles (IDPs). Chemical compositions of chondrite and IDP smectites vary widely, and include the Mg# of the Griffith saponite (i.e. its octahedral cations), but they typically have lower $Al_2O_3$ contents, and higher $Cr_2O_3$ (e.g., Hutchison and Alexander, 1987; Alexander et al., 1988; Rietmeijer, 1991; Sakamoto et al., 2010; Tomeoka and Onishi, 2011). Unlike the Griffith saponite , chondritic smectites generally have Na as their dominant interlayer cations.

Ferromagnesian tri-octahedral smectites can also form in other environments, including as direct precipitates and diagenetic products in alkaline and evaporitic settings (e.g., Jones and Weir, 1983; Hover et al. 1999; Chukanov et al. 2003; Bristow et al. 2009). These formation mechanisms are not relevant to the formation of the Griffith saponite (Neuerburger, 1951, 1953; McCulloh et al. 2002), but may be significant for Mars in general (Bristow and Milliken 2011) and the Sheepbed mudstone in particular (Grotzinger et al. 2013).

## Implications for Clay Minerals in Yellowknife Bay, Gale Crater, Mars

Data developed here confirm that the clay minerals detected by CheMin in the Sheepbed mudstone are tri-octahedral smectites, likely saponites (Vaniman et al., 2014), and provide constraints on their crystal chemistry, oxidation state, and possible mode of origin. The smectite minerals in the Sheepbed mudstone are known primarily by their X-ray diffraction properties (Vaniman et al., 2014), and the Griffith saponite is a partial analog to the Sheepbed smectite minerals. The octahedral layers of the Griffith saponite and the Sheepbed smectites are similar in size, and thus in content of octahedrally coordinated cations, as shown by the similarities of their 02$\ell$ diffraction bands. The location and shape of a smectite's 02$\ell$ diffraction bands vary according to whether the octahedral cation sites are all filled or not (tri-octahedral versus di-octahedral), and the specific identities of those cations (Fig. 9). The locations of the Griffith saponite 02$\ell$ diffraction bands, consistent with fully tri-octahedral smectites rich in iron, are consistent with their chemical compositions. Smectites in the Sheepbed mudstone have 02$\ell$ diffraction bands of similar shapes and locations to those of the Griffith saponite; by analogy it seems likely that the Sheepbed smectites are ferrian saponites.

The XRD behavior Griffith saponite under humid and dry environmental conditions provides clues for the differences in locations and widths of the Sheepbed 001 diffraction peaks. In general, differences among the 001 diffractions arise primarily from differences in interlayer

material (e.g., $H_2O$, cations, and molecular species), The Griffith saponite samples all have sharp 001 diffraction peaks; after correction for Lorentz polarization, these peaks lie at ~15 Å in humid air, at ~12.8 Å after desiccation in dry $N_2$, and at ~10 Å after desiccation on mild heating in dry $N_2$, a variation consistent with progressive loss of interlayer $H_2O$, with no change in interlayer cation. The Sheepbed saponite clay minerals have broad 001 diffraction peaks at ~10 and ~13.2 Å (corrected for Lorenz polarization) for John Klein and Cumberland, respectively. The same explanation can be used for the Sheepbed saponites, but it seems unlikely that the only difference between John Klein and Cumberland is the relative abundance of interlayer $H_2O$. Alternate, more viable explanations include differences in interlayer cations (e.g., Mg versus Ca) and pillaring. Interlayer material in smectites can reflect the smectite's formation conditions and can be modified extensively by chemical exchange and reactions long after the smectites formed. Differences in formation and/or post-formation environments are in fact implied by variability in the amount of Ca-sulfate veins associated with the two martian saponites. Thus, the interlayer material in Sheepbed saponites retains clues to its formation and subsequent chemical processing, which may be understood through laboratory experiments on ferrian saponites.

The geological setting of Griffith saponite formation is also similar, but not identical, to that of the Sheepbed smectites in Yellowknife Bay. In both locations, the saponites formed in, and from, rocks of basaltic composition; and in both, olivine was replaced by the smectite (Vaniman et al., 2014). However, there are some differences. First, the host rocks for the saponites are not identical; both are of basaltic composition, but the Griffith saponite described here is from massive basalt while the Sheepbed smectites are in basaltic sediment. However, Griffith saponite is also reported in basaltic sediments of the Topanga Canyon Formation (Neuerburg, 1953); these occurrences are under investigation. The difference between massive basalt and basaltic sediment may be unimportant chemically, but may be significant in terms of reaction rates (i.e., porosity, permeability, and specific surface areas). Second, the Sheepbed smectites are inferred to have formed (and/or been deposited) in diagenesis of lacustrine deposits (Grotzinger et al., 2004), while the Griffith saponite formed (apparently) during diagenesis in a marine environment (McCulloh et al., 2002). Differences in diagenetic environment could well account for some of the inferred differences in smectite interlayer compositions. Third, some Griffith saponite formed by replacement of glassy mesostasis material, but there is no evidence that smectite formation in Sheepbed mudstone consumed amorphous material. The amorphous

material in the Sheepbed is poorly characterized, and its abundances are difficult to constrain through models of CheMin data because of the width of the amorphous material's XRD peaks (Vaniman et al. 2014; Morris et al., 2013), so the significance of this difference is not clear. Finally, diagenesis of the Sheepbed mudstone apparently produced a significant proportion of magnetite ($Fe_3O_4$), although an igneous origin cannot be excluded. Magnetite is detected for the AMNH 89172 sample, but the oxide is associated with the basaltic separate and not the Griffith saponite separate.

Our XRD and VNIR measurements on the Griffith saponite provide a link between the XRD results for the smectite analyzed at Yellowknife Bay and the Fe-Mg smectites detectable from martian orbit by VNIR hyperspectral imaging instruments, i.e. the Compact Imaging Spectrometer for Mars (CRISM) instrument on the NASA Mars Reconnaissance Orbiter (Murchie et al., 2007) and the Observatoire pour la Mineralogie, l'Eau, les Glaces et l'Activité (OMEGA) instrument on the Mars Express orbiter (Bibring et al., 2005). Note, however, that the Sheepbed saponites do not constitute ground truth for orbital observations because clay minerals are not detected at the Sheepbed location (e.g., Milliken et al., 2010).

In CRISM spectra, Fe-Mg smectites are identified by the presence of spectral features centered near 1.9 μm (molecular $H_2O$), near 2.3 μm (2.29 - 2.32 μm), and near 2.4 μm (e.g., Ehlmann et al., 2009). The spectral band near 1.4 μm should be, but is not always, detected (Ehlmann et al., 2009). For the ~2.3 μm band, a center near 2.29 μm is inferred to represent $(Fe^{3+})_2$-OH in di-octahedral smectite (nontronite), and a band centered near 2.31 – 2.32 μm is inferred to represent $(Fe^{3+},Fe^{2+},Mg)_3$-OH in low-Fe tri-octahedral saponite (SapCa1) and hectorite (a Li-bearing smectite). A band centered near 2.30 μm is assigned to Fe-Mg smectite without specification of either the Fe redox state or the number of cation sites filled in the octahedral layers (e.g., Ehlmann et al., 2009). Our results for Griffith saponite show that the smectite detected at Yellowknife Bay by XRD and the smectite detections by CRISM and OMEGA that have band centers in the range 2.30 to 2.32 μm are all candidates for assignment to ferrian saponite with a range of $Fe^{3+}/\Sigma Fe$ values. VNIR detections having band centers near 2.30 μm and 2.32 μm are the most oxidized and reduced, respectively.

**Acknowledgments**

We are grateful to Dr. George Harlow and the American Museum of Natural History (New York) for a sample of the Griffith saponite. Our study was assisted by D.K. Ross (EMP analyses) of Jacobs Engineering, at the Johnson Space Center. We are grateful to the ARES Division, Johnson Space Center for access to the SX-100 microprobe under a cooperative agreement with the LPI. Reviews by M.D. Dyar and J. Bridges were constructive and helpful. This work was supported by NASA grants through the Mars Science Laboratory Mission. LPI Contribution #1xxx.

## REFERENCES

Agresti, D.G., Dyar, M.D., and Schaefer, M.W. (2006) Velocity scales for Mars Mössbauer data, *Hyperfine Interactions*, 170, 67-74.

Agresti, D.G., and Gerakines, P.A. (2009) Simultaneous fitting of Mars Mössbauer data, *Hyperfine Interactions*, 188, 113-120.

Alexander, C.M.O'D., Barber, D. J., and Hutchison, R. (1989) The microstructure of Semarkona and Bishunpur. *Geochimica et Cosmochimica Acta,* 53, 3045–3057.

Anderson, R.B., and Bell, J.F. III (2010) Geologic mapping and characterization of Gale Crater and implications for its potential as a Mars Science Laboratory landing site. *Mars* 5, 76-128.

Anderson, R.C., Jandura, L., Okon, A.B., Sunshine, D., Roumeliotis, C., Beegle, L.W., Hurowitz, J., Kennedy, B., Limonadi, D., McCloskey, S., Robinson, M., Seybold, C., and Brown, K. (2012) Collecting samples in Gale Crater; an overview of the Mars Science Laboratory sample acquisition, sample handling and processing system. *Space Science Rev*iews, 170, 57-75.

April, R.H., and Keller, D.M. (1992) Saponite and vermiculite in amygdales of the Granby basaltic tuff, Connecticut Valley. *Clays and Clay Minerals,* 40, 22-31.

Badaut, D., Besson, G., Decarreau, A., and Rautureau, R. (1985) Occurrence of a ferrous, trioctahedral smectite in recent sediments of Atlantis II Deep, Red Sea. *Clay Minerals,* 20, 389-404.

Bibring, J.-P., Langevin, Y., Gendrin, A., Gondet, B., Poulet, F., Berthe, M., Soufflot, A., Arvidson, R., Mangold, N., Mustard, J., and Drossart, P. (2005, Mars surface diversity as revealed by the OMEGA/Mars Express observations, *Science,* 307, 1576-1581.

Bischoff, J.L. (1972) A ferroan nontronite from the Red Sea geothermal system. *Clays and Clay Minerals,* 20, 217-223.

Bish, D.L., Carey, J.W., Vaniman D.T., and Chipera, S.J. (2003) Stability of hydrous minerals on the martian surface. *Icarus,* 164, 96–103

Blake, D.F., Vaniman, D., Achilles, C., Anderson, R., Bish, D., Bristow, T., Chen,, C., Chipera, S., Crisp, J., Des Marais, D., Downs, R.T., Farmer, J., Feldman, S., Fonda, M., Gailhanou, M., Ma, H., Ming, D.W., Morris, R.V., Sarrazin, P., Stolper, E., Treiman, A., and Yen, A. (2012) Characterization and calibration of the CheMin mineralogical instrument on Mars Science Laboratory. *Space Science Reviews,* 170, 341-399.

Borggaard, O., Lindgren, H.B., and Mørup S. (1982) Oxidation and reduction of structural iron in chlorite at 480°C. *Clays and Clay Minerals,* 30, 353-364.

Bristow, T.F., Kennedy, M.J., Derkowskia, A., Droser, M.L., Jiang, G., and Creaser, R.A. (2009) Mineralogical constraints on the paleoenvironments of the Ediacaran Doushantuo Formation. *Proceedings National Academy of Sciences (U.S.A.),* 106, 13190-13195.

Bristow, T.F., and Milliken, R.E. (2011) Terrestrial perspective on authigenic clay mineral production in ancient martian lakes. *Clays and Clay Minerals,* 59, 339-358.

Cashion, J.D., Gates W.P., and Thomson A. (2008), Mössbauer and IR analysis of iron sites in four ferruginous smectites, *Clay Minerals*, *43*, 83-93.

Changela, H.G., and Bridges, J.C. (2011) Alteration assemblages in the nakhlites: Variation with depth on Mars. *Meteoritics and Planetary Science,* 45, 1847–1867.

Chemtob, S. M., Nickerson, R. D., and Catalano, J. D. (2014) Ferrous iron smectites and their oxidative products: Implications for clay formation and alteration on Mars. *Lunar and Planetary Science Conference* **45th**, Abstract #1193.

Chukanov, N.V., Pekov, I.V., Zadov, A.E., Chukanova, V.N., and Myokkel, S. (2003) Ferrosaponite $Ca_{0.3}(Fe^{2+},Mg,Fe^{3+})_3(Si,Al)_4O_{10}(OH)_2 \cdot 4H_2O$: A new trioctahedral smectite. *Zapiski Vserossiyskogo Mineralogicheskogo Obshchestva,* 132, 68-74 (in Russian).

Critelli, S., and R. V. Ingersoll (1995) Interpretation of neovolcanic versus palaeovolcanic sand grains: an example from Miocene deep-marine sandstone of the Topanga Group (Southern California), *Sedimentology,* 42, 783-804.

Delvigne, J.E. (1998) *Atlas of Micromorphology of Mineral Alteration and Weathering. Canadian Mineralogist Special Publication 3*. Mineralogical Association of Canada, Ottawa Canada.

Ehlmann, B.L., Mustard, J.F., Swayze, G.A., Clark, R.N., Bishop, J.L., Poulet, F., Des Marias, D.J., Roach, L.H., Milliken, R.E., Wray, J.J., Barnouin-Jah, O., and Murchie, S.L. (2009) Identification of hydrated silicate minerals on Mars using MRO-CRISM: Geologic context near Nili Fossae and implications for aqueous alteration, *Journal of Geophysical Research,* 114, E00D08, doi:10.1029/2009JE003339.

Eggleton, R.A. (1984) Formation of iddingsite rims on olivine: a transmission electron microscope study. *Clays and Clay Minerals,* 32, 1-11.

Farmer, V.C., Russell, J.D., MacHardy, W.J., Newman, A.C.D., Ahlrichs, J.L., and Rimsaite, J.Y.H. (1971) Evidence for loss of protons and octahedral iron from oxidized biotites and vermiculites: *Mineralogical Magazine,* 38, 121-137.

Faust, G.T. (1955) Thermal analysis and x-ray studies of griffithite. *Journal of the Washington Academy of Sciences,* 45, 66-70.

Fialips, C.-I., Huo, D., Yan, L., Wu, J., and Stucki, J.W. (2002) Effect of Fe oxidation state on the IR spectra of Garfield nontronite, *American Mineralogist,* 87, 630-641.

Fleischer, M. (1955) New Mineral Names, *American Mineralogist,* 40, 941-944.

Gandia, L.M., Gil, A., Vicente, M.A., and Belver, C. (2005) Dehydrogenation of ethylbenzene on alumina-pillared Fe-rich saponites. *Catalysis Letters,* 101, 229-234.

Gates, W.P., Slade P. G., Manceau A., and Lanson B. (2002), Site occupancies by iron in nontronites, *Clays Clay Minerals*, *50*, 223-239.

763 Grotzinger, J.P., Sumner, D., Kah, L., Stack, K., Gupta, S., Edgar, L., Rubin, D., Lewis, K.,
764 Scheiber, J., Mangold, N., Milliken, R., Conrad, P., DesMarais, D., Farmer, J., Siebach, K.,
765 Calef, F., Hurowitz, J., McLennan, S., Ming, D., Vaniman, D., Crisp, J., Vasavada, A.,
766 Edgett, K., Malin, M., Blake, D., Gellert, R., Mahaffy, P., Wiens, R., Maurice, S., Grant, J.,
767 Purdy, S., Anderson, R., Beegle, L., Arvidson, R., Hallet, B., Sletten, R., Rice, M., Bell, J.,
768 Griffes, J., Ehlmann, B., Bristow, T., Palucis, M., Dietrich, W., Dromart, G., Eigenbrode, J.,
769 Fraeman, A., Hardgrove, C., Herkenhoff, K., Jandura, L., Kocurek, G., Lee, S., Leshin, L.,
770 Leveille, R., Limonadi, D., Maki, J., McCloskey, S., Meyer, M., Minitti, M., Oehler, D.,
771 Okon, A., Newsom, H., Parker, T., Rowland, S., Squyres, S., Steele, A., Stolper, E.,
772 Summons, R., Treiman, A., Williams, R., and Yingst, A. (2014) A habitable
773 fluvio˜ lacustrine environment at Yellowknife Bay, Gale Crater, Mars. To *Science,* 343,
774 124277

775 Güven, N. (1988) Smectites. 497-600 in *Hydrous Phyllosilicates (Exclusive of Micas)*, S.W.
776 Bailey ed., *Reviews in Mineralogy 19*, Mineralogical Society of America, Washington DC.

777 Hoots, H.W. (1931) Geology of the eastern part of the Santa Monica Mountains, Los Angeles
778 County, California, *U. S. Geological Survey Professional Paper 165-C*. p. 83-134.

779 Hover, V.C., Walter, L.M., Peacor, D.R., and Martini, A.M. (1999) Mg-smectite authigenesis in
780 a marine evaporative environment, Salina Ometepec, Baja California. *Clays and Clay*
781 *Minerals,* 47, 252-268.

782 Hutchison, R., and Alexander, C.M.O'D. (1987) The Semarkona meteorite: First recorded
783 occurrence of smectite in an ordinary chondrite, and its implications. *Geochimica et*
784 *Cosmochimica Acta,* 51, 1875-1882.

785 Jones, B.F., and Weir, A.H. (1983) Clay minerals of Lake Abert, an alkaline, saline lake. *Clays*
786 *and Clay Minerals,* 31, 161-172

787 King, T.V.V., and Clark, R.N. (1989) Spectral characteristics of chlorites and Mg-serpentines
788 using high-resolution reflectance spectroscopy. *Journal of Geophysical Research,* 94,
789 13,997-14,008.

790 Klingelhöfer, G., Morris, R.V., Bernhardt, B., Rodionov, D., de Souza, P.A.Jr., Squyres, S.W.,
791 Foh, J., Kankeleit, E., Bonnes, U., Gellert, R., Schröder, C., Linkin, S., Evlanov, E., Zubkov,

B., and Prilutski, O. (2003) Athena MIMOS II Moessbauer spectrometer investigation, *Journal of Geophysical Research,* 108, 8067, doi:10.1029/2003JE002138.

Kodama H., DeKimpe C.R., and Dejou J. (1988) Ferrian saponite in a gabbro saprolite at Mont Mégantic, Quebec. *Clays and Clay Minerals,* 36, 102-110.

Kohyama, N., Shimoda S., and Sudo T. (1973) Iron-rich saponite (ferrous and ferric forms), *Clays Clay Minerals*, *21*, 229-237.

Kohyama, N., and Sudo T. (1975) Hisingerite occurring as a weathering product of iron-rich saponite, *Clays Clay Minerals*, *23*, 215-218.

Komadel, P. (2003) Chemically modified smectites. *Clay Minerals,* 38, 127-138.

Komadel, P., and Madejova, J. (2006) Acid activation of clay minerals. *Developments in Clay Science,* 1, 263-287.

Komadel, P., Madejova, J., and Stucki, J.W. (1995), Reduction and reoxidation of nontronite: Questions of reversibility, *Clays Clay Minerals*, 43, 105-110.

Komadel, P., Madejova, J., Laird, D.A., Xia, Y., and Stucki, J.W. (2000) Reduction of Fe(III) in griffithite. *Clay Minerals,* 35, 625-634.

Köster, H.M., Erlicher U., Gilg, H.A., Jordan, R., Murad, E., and Onnich, K. (1999) Mineralogical and chemical characteristics of five nontronites and Fe-rich smectites. *Clay Minerals,* 34, 579–599.

Larsen, E. S., and G. Steiger (1917), Griffithite, A member of the chlorite group, *American Mineralogist,* 2, 54.

Larsen, E. S., and G. Steiger (1928), Dehydration and optical studies of alunogen, nontronite, and griffithite, *American Journal of Science*, 15, 1-19.

Lear, P.R., and Stucki, J.W. (1985) Role of structural hydrogen in the reduction and reoxidation of iron in nontronite. *Clays and Clay Minerals,* 33, 539-545.

Manceau, A., Drits V.A., Lanson, B., Chateigner, D., Wu, J., Huo, D., Gates, W.P., and Stucki, J.W. (2000) Oxidation-reduction mechanism of iron in dioctahedral smectites: II. Crystal chemistry of reduced Garfield nontronite, *American Mineralogist,* 85, 153-172.

Mas, A., Meunier, A., Beaufort, D., Patrier, P., and Dudoignon, P. (2008) Clay minerals in basalt-hawaiite rocks from Mururoa Atoll (French Polynesia). I. Mineralogy. *Clays and Clay Minerals,* 56, 711–729.

McCulloh, T.H., Fleck, R.J., Denison, R.E., Beyer, L.A., and Stanley, R.G. (2002) *Age and Tectonic Significance of Volcanic Rocks in the Northern Los Angeles Basin, California.* USGS Prof. Paper 1669, 24 p.

Milliken, R.E. and Bish, D.L. (2010) Sources and sinks of clay minerals on Mars. *Philosophical Magazine,* 90, 2293-2308.

Milliken, R. E., J. P. Grotzinger, and B. J. Thomson (2010), Paleoclimate of Mars as captured by the stratigraphic record in Gale Crater, *Geophysical Research Letters*, 37, L04201, doi:04210.01029/02009GL041870.

Ming, D.W., Archer, P.D.Jr., Glavin, D.P., Eigenbrode, J.L., Franz, H., Sutter, B., Brunner, A.E., Stern, J.C., Freissinet, C., McAdam, A.C., Mahaffy, P.R., Cabane, M., Coll, P., Campbell, J.L., Atreya, S.K., Niles, P.B., Bell, J.F.III, Brinckerhoff, W.B., Buch, A., Conrad, P.G., Des Marais, D.J., Ehlmann, B.L., Fairen, A.G., Farley, K., Flesch, G.J., Gellert, R., Grant, J.A., Grotzinger, J.P., Gupta, S., Herkenhoff, K.E., Hurowitz, J.A., Leshin, L.A., Lewis, K.W., McLennan, S.M., Miller, K.E., Moersch, J., Morris, R.V., Navarro-González, R., Pavlo, A.A., Perrett, G., Pradler, I., Squyres, S.W., Summons, R., Steele, A., Stolper, E.M., Sumner, D.Y., Szopa, C., Teinturier, S., Trainer, M.G., Treiman, A.H., Vaniman, D.T., Vasavada, A.R., Webster, C.R., Wray, J.J., Yingst, R.A., and the MSL Science Team (2014) Volatile and organic compositions of a sedimentary rock in Yellowknife Bay, Gale crater, Mars. *Science,* 343, 1245267.

Moore, D.M., and Reynolds R.C. Jr. (1997) *X-Ray Diffraction and the Identification and Analysis of Clay Minerals*, 378 pp., Oxford University Press, Oxford.

Morris, R.V., Klingelhöfer, G., Schröder, C., Rodionov, D. S., Yen, A. S., Ming, D. W., de Souza, P. A. Jr., Wdowiak, T., Fleischer, I., Gellert, R., Bernhardt, B., Bonnes, U., Cohen, B. A., Evlanov, E. N., Foh, J., Gütlich, P., Kankeleit, E., McCoy, T. J., Mittlefehldt, D. W., Renz, F., Schmidt, M. E., Zubkov, B., Squyres, S. W., and Arvidson, R. E. (2006) Mössbauer mineralogy of rock, soil, and dust at Meridiani Planum, Mars: Opportunity's

journey across sulfate-rich outcrop, basaltic sand and dust, and hematite lag deposits. *Journal of Geophysical Research,* 111, E12S15.

Morris, R.V., Klingelhöfer, G., Schröder, C., Fleischer, I., Ming, D. W., Yen, A. S., Gellert, R., Arvidson, R. E., Rodionov, D. S., Crumpler, L. S., Clark, B. C., Cohen, B. A., McCoy, T. J., Mittlefehldt, D. W., Schmidt, M. E., de Souza, P. A. Jr., and Squyres, S. W. (2008) Iron mineralogy and aqueous alteration from Husband Hill through Home Plate at Gusev Crater, Mars: Results from the Mössbauer instrument on the Spirit Mars Exploration Rover. *Journal of Geophysical Research,* 113, E12S42.

Morris, R.V., Ming, D.W., Blake, D.F., Vaniman, D.T., Bish, D.L., Chipera, S.J., Downs, R.T., Treiman, A.H., Yen, A.S., Achilles, C.N., Anderson, R.C., Bristow, T.F., Crisp, J.A., Des Marais, D.J., Farmer, J.D., Morookian, J.M., Morrison, S.M., Rampe, E.B., Sarrazin, P.C., Spanovich, N., Stolper, E.M., & the MSL team (2013) The amorphous component in martian basaltic soil in global perspective from MSL and MER missions. *Lunar and Planetary Science Conference,* 44th. Abstr. #1653.

Murchie, S., Arvidson, R., Bedini, P., Beisser, K., Bibring, J.-P., Bishop, J., Boldt, J., Cavender, P., Choo, T., Clancy, R.T., Darlington, E.H., Des Marais, D., Espiritu, R., Fort, D., Green, R., Guinness, E., Hayes, J., Hash, C., Heffernan, K., Hemmler, J., Heyler, G., Humm, D., Hutcheson, J., Izenberg, N., Lee, R., Lees, J., Lohr, D., Malaret, E., Martin, T., McGovern, J.A., Morris, R., Mustard, J., Pelkey, S., Rhodes, E., Robinson, M., Roush, T., Schaefer, E., Seagrave, G., Seelos, F., Silverglate, P., Slavney, S., Smith, M., Shyong, W.-J., Strohbehn, K., Taylor, H., Thompson, P., Tossman, B., Wirzburger, M., and Wolff, M. (2007) Compact Reconnaissance Imaging Spectrometer for Mars (CRISM) on Mars Reconnaissance Orbiter (MRO), *Journal of Geophysical Research,* E05S03, doi:10.1029/2006JE002682.

Neumann, A., Sander, M., and Hofstetter, T.B. (2011) Redox properties of structural Fe in smectite clay minerals, 361-379 in *Aquatic Redox Chemistry*, P.G. Tratnyek, T.J. Grundl, and S.B. Haderlein, eds. ACS Symposium Series; American Chemical Society: Washington, DC.

Newman, A.C.D., and Brown, G. (1987) The chemical constitution of clays. p. 2-128 in A.C.D. Newman (ed.) *Chemistry of Clays and Clay Minerals, Mineralogical Society Monograph No. 6*. John Wiley & Sons NY.

878 Neuerburg, G.J. (1951) Minerals of the eastern Santa Monica Mountains, Los Angeles City.
879 *American Mineralogist,* 36,156-160.

880 Neuerburg, G.J. (1953) *Geology of the Griffith Park Area, Los Angeles County, California.*
881 California Division of Mines Special Report 33, 29 p.

882 O'Hanley, D.S. (1996) *Serpentinites: Records of Tectonic and Petrologic History*. Oxford
883 University Press, NY. 277 p.

884 Parra, M., Delmont P., Ferrange A., Latouche C., Pons J.C., and Puechmaille C. (1985) Origin
885 and evolution of smectites in recent marine sediments of the NE Atlantic, *Clay Minerals*, *20*,
886 335-346.

887 Parthasarathy, G., Choudary, B.M., Sreedhar, B., Kunwar, A.C., and Srinivasan, R. (2003)
888 Ferrous saponite from the Deccan Trap, India, and its application in adsorption and
889 reduction of hexavalent chromium. *American Mineralogist,* 88, 1983-1988.

890 Pecuil, T.E., Wampler, J.M., and Weaver, C.E. (1966) A study of iron in clay minerals using
891 Mössbauer spectroscopy. *Clays and Clay Minerals,* 15, 143-144.

892 Rancourt, D.G., Tume, P., and Lalonde, A.E. (1993). Kinetics of the ($Fe^{2+}$ + $OH^{-}$) mica → ($Fe^{3+}$
893 + $O^{2-}$) mica + H oxidation reaction in bulk single-crystal biotite studied by Mössbauer
894 spectroscopy. *Physics and Chemistry of Minerals,* 20, 276-284.

895 Reynolds, R.C.Jr. (1986) The Lorentz-polarization factor and preferred orientation in oriented
896 clay aggregates, *Clays Clay Minerals*, *34*, 359-367.

897 Rietmeijer, F.J.M. (1991) Aqueous alteration in five chondritic porous interplanetary dust
898 particles. *Earth and Planetary Science Letters* 102, 148-157.

899 Robert, C., and Goffé, B. (1993) Zeolitization of basalts in subaqueous freshwater settings: Field
900 observations and experimental study. *Geochimica et Cosmochimica Acta* **57**, 3597-3612.

901 Rodriguez, M.A.V., Suarez Barrios, M., López González, J.D., and Banares Muñoz, M.A. (1994)
902 Acid activation of a ferrous saponite (griffithite): Physico-chemical characterization and
903 surface area of the products obtained. *Clays and Clay Minerals* **42**, 724-730.

904 Rodriguez, M.A.V., López González, J.D., and Banares Muñoz, M.A. (1995) Preparation of
905 microporous solids by acid treatment of a saponite. *Microporous Materials* **4**, 251–264

Ross, C.S. (1958) Review of the relationships in the montmorillonite group of clay minerals. *Clays and Clay Minerals* **7**, 225-229.

Sakamoto, K., Nakamura, T., Noguchi, T., and Tsuchiyama, A. (2011) A new variant of saponite-rich micrometeorites recovered from recent Antarctic snowfall. *Meteoritics & Planetary Science* **45**, 220–237.

Scheidegger, K.F., and Stakes D.S. (1977) Mineralogy, chemistry, and crystallization sequence of clay minerals in altered tholeitic basalts from the Peru trench, *Earth and Planet. Sci. Letters*, *36*, 413-422

Schwenzer, S.P., Abramov, O., Allen, C.C., Bridges, J.C., Clifford, S.M., Filiberto, J., Kring, D.A., Lasue, J., McGovern, P.J., Newsom, H.E., Treiman, A.H., Vaniman, D.T., Wiens, R.C., and Wittmann, A. (2012) Gale Crater: Formation and post-impact hydrous environments. *Planetary and Space Science* **70**, 84–95.

Stucki, J.W. (2006), Chapter 8: Properties and Behaviour of Iron in Clay Minerals, in *Developments in Clay Science*, edited by F. Bergaya, B. K. G. Theng and L. Gerhard, pp. 423-475, Elsevier.

Treiman, A.H., and Lindstrom, D.J. (1997) Trace element geochemistry of martian iddingsite in the Lafayette meteorite. *Journal of Geophysical Research* **102**, 1953-1963.

Treiman, A.H., Barrett, R.A. and Gooding, J.L. (1993) Preterrestrial aqueous alteration of the Lafayette (SNC) meteorite. *Meteoritics* **28**, 86-97.

Vaniman, D.T., Bish, D.L., Blake, D.F., Chipera, S.J., Morris, R.V., Ming, D.W., Sarrazin, P.C., Treiman, A.H., Downs, R.T., Achilles, C.N., Morrison, S.M., Yen, A.S., Bristow, T.F., Morookian, J.M., Farmer, J.D., Crisp, J.A., Rampe, E.B., Stolper, E.M., Spanovich, N., and the MSL Team (2014) Mineralogy of a mudstone on Mars. *Science* 343, 1243480.

Vicente, M.A., Bañares-Muñoz, M.A., Suarez, M., Pozas, J.M., Lopez-Gonzalez, J.D., Santamaria, J., and Jiminez-Lopez, A. (1996) Pillaring of a high iron content saponite with aluminum polycations: Surface and catalytic properties. *Langmuir* **12**, 5143-5147.

Vicente, M.A., Suarez, M., Bañares-Muñoz, M.A., and Pozas, J.M.M. (1997) Characterization of the solids obtained by pillaring of griffithite (high iron content saponite) with A1-oligomers. *Clays and Clay Minerals* **45**, 761-768.

Vicente, M.A., Suarez, M., Bañares-Muñoz, M.A., and Pozas, J.M.M. (1998) Reduction of Fe(III) in a high-iron saponite. Pillaring of the reduced samples with $Al_{13}$ oligomers. *Clay Minerals* **33**, 213–220.

Vicente-Rodrigues, M.A., Suarez, M., Bañares-Muñoz, M.A., and Lopez-Gonzalez, J.D. (1996) Comparative FT-IR study of the removal of octahedral cations and structural modifications during acid treatment of several silicates. *Spectrochimica Acta Part A: Molecular and Biomolecular Spectroscopy* **52**, 1685–1694.

Walters, S.G., and Ineson, P.R. (1983) Clay minerals in the basalts of the South Pennines. *Mineralogical Magazine* **47**, 21-26.

Wilson, M.J. (2004) Weathering of the primary rock-forming minerals: processes, products and rates *Clay Minerals* **39**, 233-266.

Wray, J.J. (2013) Gale crater: the Mars Science Laboratory/ Curiosity Rover landing site. *International Journal of Astrobiology* **12**, 25–38.

Yerkes, R.F., and Campbell, R.H. (1979) *Stratigraphic Nomenclature of the Central Santa Monica Mountains, Los Angeles County, California*. U.S. Geological Survey Bulletin 1457-E. U.S. Government Printing Office.

Zolensky, M.E., Krot, A.N., and Benedix G. (2008) Record of low-temperature alteration in asteroids. *Reviews in Mineralogy & Geochemistry* **68**, 429-462.

953

954 # Figure Captions

955 **Figure 1.** MSL Results. **(a)** X-ray diffraction patterns compared for the John Klein and Cumberland samples
956 (CheMin on Mars, CoKα radiation, Vaniman et al., 2013). Similarity between the mudstone samples is evident
957 but there are notable differences in the clay mineral 001 spacing (corrected for Lorentz polarization) at ~7.7° 2θ
958 (13.2 Å) in Cumberland and at ~10° 2θ (10 Å) in John Klein, as well as stronger reflections at 17° 2θ (6 Å) for
959 bassanite and 29.7° 2θ (3.5 Å) for anhydrite plus olivine in John Klein (Vaniman et al., 2013). **(b)** Detail of the
960 02ℓ diffraction bands for John Klein and Cumberland samples. Note that band peaks are at 4.59 Å.

961

962 **Figure 2.** Macroscopic optical images of saponite-bearing samples from Griffith Park, CA; reference cube is 1
963 cm on each side. **(a)** MU bulk sample. **(b)** MU sample, saponite filling ellipsoidal vesicle (center), and coarse-
964 grained platy saponite (top, arrow) possibly replacing an olivine phenocryst (see Fig. 3c). **(c)** MU sample,
965 coarse-grained platy saponite in center, inferred as a replacement of an olivine phenocryst (see Fig. 3c). **(d)**
966 CASGP1, bulk sample. Dark patches are vesicles filled with saponite; light-toned areas at top of image are
967 ellipsoids of silica filling vesicles. **(e)** CASGP1, detail of fine-grained saponite (center of image) as a veinlet or
968 crack fill, and exterior to a quartz globule (pale green, to left of image).

969

970 **Figure 3.** Textures of Griffith smectites and host basalts. Substances include: sp, saponite; sp-c, coarse-grained
971 saponite; sp-f, fine-grained saponite; pl, plagioclase; px pyroxene; and me, mesostasis. **(a)** BSE image of
972 saponite extracted from a filled vesicle. AMNH 89172. Note abundant lenticular voids, characteristic of
973 saponite dehydration. Arrow denotes radiating lenticular voids. **(b)** Secondary electron image of saponite
974 extracted from a filled vesicle. AMNH 89172. Note abundant lenticular voids, characteristic of saponite
975 dehydration, and radiating sprays of saponite flakes. **(c)** BSE image of saponite pseudomorph after a euhedral
976 olivine crystal. AMNH 89172. Arrows denote large saponite flakes (cleavages) perpendicular to large cracks,
977 which represent cleavage planes ({001}, {010}) in the original olivine crystal. **(d)** BSE image, typical texture of
978 basalt. AMNH 89172. Plagioclase euhedra with interstitial augite pyroxene (sub-ophitic texture) and mesostasis
979 with laths of ilmenite. **(e)** BSE image, vesicle filled with saponite and host basalt. MU sample. **(f)** BSE image,
980 saponite pseudomorph after olivine, and mesostasis with ilmenite laths. MU sample. **(g)** BSE image, mesostasis
981 area rich in saponite, with dendritic and hollow crystals of titanomagnetite. MU sample. **(h)** BSE image, vesicle
982 fill with central coarse-grained saponite, and outer fine-grained saponite. CASGP1. **(i)** BSE image, portion of a

983 filled vesicle, with spherules of quartz (s) in fine-grained saponite. CASGP1. **(j)** BSE image, saponite
984 pseudomorph after olivine, and mesostasis with ilmenite laths. CASGP1.
985
986 **Figure 4.** Compositions, anhydrous silicate minerals. EMP chemical analyses of pyroxenes **(a)** and feldspars
987 **(b)** in saponite -bearing samples. The pyroxenes, plotted in the pyroxene quadrilateral, are all magnesian sub-
988 calcic augites. The feldspars are all plagioclases of intermediate compositions (labradorite to andesine), except
989 for two analytical spots with significant potassium. See Appendix 1.
990
991 **Figure 5.** Comparison of chemical and Fe redox data for Griffith saponite reported in the literature and
992 analyzed in this study (Table 3). (a) $CaO/FeO_T$ versus $MnO/FeO_T$. (b) $Fe^{3+}/\sum Fe$ versus $MnO/FeO_T$. Data from
993 Larsen and Steiger (1917) arbitrarily plotted at $MnO/FeO_T = 0.015$ because no MnO analysis was reported.
994
995 **Figure 6**. Mössbauer spectra (room temperature) of hand-picked Griffith saponite separates. **(a)**, **(b)**, and **(c)** are
996 coarse-grained globules (vesicle fill or olivine replacement) and **(d)** is a fine-grained vein fill. TC = Total
997 Counts; BC = Baseline Counts.
998
999 **Figure 7.** XRD patterns obtained in transmission geometry (CheMin-IV instrument) from powders of Griffith
000 saponite derived from veins and globules hand-picked from basalt. Coarse-grained, dark globules (~1 mm) and
001 brown fine-grained vein fill from sample CASCP1 and coarse grained, dark globules (2-3 mm) from sample
002 AMNH 89172. The presence of sharp, strong 00$\ell$ diffraction lines indicates that the Griffith saponite is highly
003 crystalline. All samples were equilibrated with lab air.
004
005 **Figure 8**. Griffith saponite from AMNH 89172 equilibrated in lab air, desiccated in dry $N_2$ gas, and re-
006 equilibrated in lab air, and re-equilibrated in lab air after heating at 220 °C in dry $N_2$ gas. The decrease in d-
007 spacing for the 00$\ell$ series upon desiccation results from removal of interlayer $H_2O$; for example the d-spacing of
008 the 001 line decreases from ~15 Å (~2 interlayer $H_2O$) to ~11.8 Å (<1 interlayer $H_2O$ on average). The position
009 of 02$\ell$ band is weakly dependent on interlayer d-spacing, and its position did not change with desiccation (~4.59
010 Å).
011

**Figure 9.** Comparison of the position of 02$\ell$ diffraction band for Griffith saponite samples with those for low-Fe saponite (SapCa-1), nontronite or ferruginous di-octahedral smectite (API-33A, PHY07, SWa-1, NAu-1, and WASCDB1), Na-montmorillonite (SWy-1 and BSDMNT1) and Ca-montmorillonite (SAz-1 and STx-1).

**Figure 10.** Visible and near-IR reflectance spectra at rooom temperature for Griffith saponite samples equilibrated in lab air. MUGPLA1_PHY, CASGP1-C, CASGP-F, and AMNH89172_PHY. **(a)** Absolute reflectance. **(b)** Continuum normalized reflectance for the MOH region (2.20 to 2.50 μm).

**Figure 11.** Visible and near-IR reflectance spectra for Griffith saponite AMNH89172_PHY at room temperature and various environmental treatments: equilibrated in lab air (blue); desiccated in dry $N_2$ gas at room temperature (dark blue); desiccated in dry $N_2$ gas at ~110 °C (magenta); desiccated in dry $N_2$ gas at ~220 °C (orange); and re-equilibrated in lab air (green). **(a)** Absolute reflectance. Continuum normalized absolute reflectance for the **(b)** HOH and MOH (1.8 to 2.5 μm) and **(c)** OH (1.30 to 1.60 μm) spectral regions.

029
030

**Table 1.** Pyroxenes from Smectite-bearing Samples, Griffith Park, CA: Chemical Compositions (EMP) And Structural Formulae to 4 Cations

| Sample | MU, L3 | | | | | | | | | |
|---|---|---|---|---|---|---|---|---|---|---|
| Anal. # | 15 | 19 | 20 | 23 | 24 | 25 | 26 | 27 | 28 | 29 |
| $SiO_2$ | 49.01 | 48.67 | 52.08 | 49.42 | 49.08 | 48.18 | 48.32 | 49.34 | 43.20 | 46.10 |
| $TiO_2$ | 1.40 | 1.03 | 0.93 | 0.64 | 1.06 | 1.68 | 1.41 | 0.55 | 1.09 | 1.23 |
| $Al_2O_3$ | 5.34 | 1.88 | 2.55 | 4.89 | 2.24 | 2.87 | 3.30 | 14.43 | 4.44 | 4.04 |
| $Cr_2O_3$ | 0.48 | 0.10 | 0.23 | 0.12 | 0.26 | 0.26 | 0.13 | 0.05 | 0.11 | 0.04 |
| FeO | 10.09 | 10.59 | 10.79 | 9.47 | 10.64 | 9.87 | 9.80 | 6.12 | 8.66 | 9.57 |
| NiO | 0.00 | 0.01 | 0.05 | 0.00 | 0.00 | 0.01 | 0.00 | 0.00 | 0.00 | 0.00 |
| MnO | 0.32 | 0.27 | 0.34 | 0.30 | 0.30 | 0.31 | 0.26 | 0.18 | 0.22 | 0.26 |
| MgO | 13.55 | 15.39 | 13.97 | 12.78 | 15.69 | 15.02 | 14.71 | 10.24 | 14.40 | 14.80 |
| CaO | 18.05 | 19.07 | 18.11 | 15.17 | 17.75 | 19.06 | 18.78 | 13.15 | 17.26 | 17.75 |
| $Na_2O$ | 0.95 | 0.28 | 0.74 | 1.04 | 0.26 | 0.34 | 0.49 | 2.60 | 1.04 | 0.89 |
| $K_2O$ | 0.05 | 0.02 | 0.00 | 0.06 | 0.00 | 0.01 | 0.00 | 0.00 | 0.01 | 0.04 |
| total | 99.22 | 97.31 | 99.79 | 93.89 | 97.28 | 97.62 | 97.20 | 96.65 | 90.42 | 94.70 |
| | | | | | | | | | | |
| Si | 1.834 | 1.858 | 1.947 | 1.951 | 1.873 | 1.835 | 1.844 | 1.854 | 1.750 | 1.792 |
| Ti | 0.039 | 0.030 | 0.026 | 0.019 | 0.030 | 0.048 | 0.041 | 0.015 | 0.033 | 0.036 |
| Al | 0.235 | 0.084 | 0.112 | 0.227 | 0.101 | 0.129 | 0.149 | 0.639 | 0.212 | 0.185 |
| Cr | 0.014 | 0.003 | 0.007 | 0.004 | 0.008 | 0.008 | 0.004 | 0.002 | 0.003 | 0.001 |
| $Fe^{2+}$ | 0.316 | 0.338 | 0.338 | 0.313 | 0.340 | 0.314 | 0.313 | 0.192 | 0.293 | 0.311 |
| Ni | 0.000 | 0.000 | 0.002 | 0.000 | 0.000 | 0.000 | 0.000 | 0.000 | 0.000 | 0.000 |
| Mn | 0.010 | 0.009 | 0.011 | 0.010 | 0.010 | 0.010 | 0.008 | 0.006 | 0.008 | 0.009 |
| Mg | 0.756 | 0.876 | 0.779 | 0.752 | 0.893 | 0.853 | 0.837 | 0.574 | 0.870 | 0.858 |
| Ca | 0.724 | 0.780 | 0.725 | 0.642 | 0.726 | 0.778 | 0.768 | 0.530 | 0.749 | 0.739 |
| Na | 0.069 | 0.021 | 0.054 | 0.080 | 0.020 | 0.025 | 0.036 | 0.189 | 0.081 | 0.067 |
| K | 0.003 | 0.001 | 0.000 | 0.003 | 0.000 | 0.000 | 0.000 | 0.000 | 0.000 | 0.002 |
| | | | | | | | | | | |
| $\Sigma\ ^{IV}$Cats* | 1.923 | 1.909 | 1.976 | 2.004 | 1.935 | 1.922 | 1.923 | 1.999 | 1.808 | 1.854 |

Samples: MU, from Minerals Unlimited; Roman numeral superscripts are site coordinations.
* $\Sigma\ ^{IV}$Cats = Si+(Al/2)+Ti-Na.

**Table 2.** Plagioclases in Smectite-bearing Samples, Griffith Park, CA: Chemical Compositions (EMP) And Structural Formulae to 5 Cations

| Sample | MU, L3 | | | | | | | | | |
|---|---|---|---|---|---|---|---|---|---|---|
| Anal. # | 1 | 2 | 3 | 6 | 12 | 13 | 14 | 33 | 34 | 35 |
| $SiO_2$ | 50.97 | 49.61 | 53.42 | 52.28 | 52.74 | 53.00 | 52.85 | 55.43 | 54.13 | 53.87 |
| $TiO_2$ | 0.07 | 0.09 | 0.01 | 0.06 | 0.10 | 0.05 | 0.28 | 0.15 | 0.14 | 0.08 |
| $Al_2O_3$ | 27.53 | 28.00 | 22.49 | 27.09 | 24.64 | 25.91 | 22.86 | 26.29 | 26.67 | 26.40 |
| $Cr_2O_3$ | 0.04 | 0.00 | 0.00 | 0.00 | 0.00 | 0.00 | 0.00 | 0.02 | 0.00 | 0.00 |
| FeO | 0.96 | 1.54 | 1.68 | 0.74 | 1.26 | 0.78 | 3.02 | 0.85 | 0.65 | 0.62 |
| NiO | 0.00 | 0.00 | 0.00 | 0.01 | 0.00 | 0.00 | 0.00 | 0.02 | 0.00 | 0.00 |
| MnO | 0.03 | 0.12 | 0.06 | 0.05 | 0.02 | 0.00 | 0.11 | 0.02 | 0.00 | 0.00 |
| MgO | 0.61 | 1.47 | 1.90 | 0.14 | 0.49 | 0.19 | 1.58 | 0.23 | 0.18 | 0.19 |
| CaO | 11.80 | 11.78 | 7.14 | 10.44 | 8.62 | 9.75 | 10.31 | 9.69 | 9.77 | 10.22 |
| $Na_2O$ | 4.41 | 3.02 | 6.72 | 5.33 | 5.62 | 5.82 | 5.43 | 4.62 | 5.70 | 5.61 |
| $K_2O$ | 0.00 | 0.01 | 0.02 | 0.01 | 0.01 | 0.00 | 0.00 | 0.00 | 0.01 | 0.02 |
| total | 96.44 | 95.64 | 93.43 | 96.16 | 93.51 | 95.50 | 96.45 | 97.30 | 97.25 | 97.00 |
| | | | | | | | | | | |
| Si | 2.394 | 2.368 | 2.546 | 2.451 | 2.541 | 2.495 | 2.480 | 2.591 | 2.506 | 2.501 |
| Ti | 0.003 | 0.003 | 0.000 | 0.002 | 0.004 | 0.002 | 0.010 | 0.005 | 0.005 | 0.003 |
| Al | 1.524 | 1.575 | 1.263 | 1.497 | 1.399 | 1.437 | 1.264 | 1.449 | 1.455 | 1.444 |
| Cr | 0.002 | 0.000 | 0.000 | 0.000 | 0.000 | 0.000 | 0.000 | 0.001 | 0.000 | 0.000 |
| Fe | 0.038 | 0.061 | 0.067 | 0.029 | 0.051 | 0.031 | 0.119 | 0.033 | 0.025 | 0.024 |
| Ni | 0.000 | 0.000 | 0.000 | 0.001 | 0.000 | 0.000 | 0.000 | 0.001 | 0.000 | 0.000 |
| Mn | 0.001 | 0.005 | 0.002 | 0.002 | 0.001 | 0.000 | 0.005 | 0.001 | 0.000 | 0.000 |
| Mg | 0.043 | 0.105 | 0.135 | 0.010 | 0.035 | 0.013 | 0.110 | 0.016 | 0.012 | 0.013 |
| Ca | 0.594 | 0.602 | 0.365 | 0.525 | 0.445 | 0.492 | 0.518 | 0.485 | 0.484 | 0.508 |
| Na | 0.402 | 0.280 | 0.621 | 0.484 | 0.524 | 0.531 | 0.494 | 0.418 | 0.512 | 0.505 |
| K | 0.000 | 0.001 | 0.001 | 0.001 | 0.000 | 0.000 | 0.000 | 0.000 | 0.001 | 0.001 |
| □□□□ | 3.918 | 3.943 | 3.809 | 3.947 | 3.940 | 3.932 | 3.744 | 4.040 | 3.961 | 3.946 |

Samples: MU, from Minerals Unlimited; Roman numeral superscripts are site coordinations.

**Table 3.** Chemical Compositions (EMP) and Structural Formulae of Saponite from Griffith Park, CA, and Others

| Sample | AMNH | | AMNH | | AMNH | | MU | | MU | | MU | | CAS | |
|---|---|---|---|---|---|---|---|---|---|---|---|---|---|---|
| Type | Vf-c | 1σ | ExOl | 1σ | Meso | 1σ | Vf-c | 1σ | ExOl | 1σ | Meso | 1σ | Vf-f | 1σ |
| $SiO_2$ | 44.63±1.34 | | 45.95±1.25 | | 45.75±1.95 | | 43.68±1.78 | | 44.20±1.27 | | 42.76±1.96 | | 43.40±1.85 | |
| $TiO_2$ | 0.01±0.01 | | 0.03±0.02 | | 0.10±0.17 | | 0.02±0.02 | | 0.09±0.18 | | 0.51±0.68 | | 0.04±0.02 | |
| $Al_2O_3$ | 8.36±0.75 | | 7.91±0.56 | | 7.91±0.44 | | 7.93±0.43 | | 7.69±0.21 | | 7.26±0.78 | | 7.10±0.39 | |
| $Cr_2O_3$ | 0.01±0.01 | | 0.02±0.02 | | 0.01±0.02 | | 0.01±0.01 | | 0.01±0.01 | | 0.01±0.03 | | 0.02±0.02 | |
| FeO | 14.87±0.52 | | 15.60±0.56 | | 16.35±1.02 | | 16.35±0.44 | | 14.80±0.30 | | 15.97±1.95 | | 13.67±0.33 | |
| NiO | -- | | -- | | -- | | 0.03±0.02 | | 0.03±0.02 | | 0.01±0.02 | | 0.06±0.02 | |
| MnO | 0.07±0.03 | | 0.08±0.02 | | 0.12±0.04 | | 0.56±0.04 | | 0.70±0.04 | | 0.68±0.06 | | 0.06±0.03 | |
| MgO | 19.00±0.91 | | 19.09±0.59 | | 18.18±0.88 | | 18.87±0.96 | | 19.45±1.05 | | 16.86±2.85 | | 18.01±0.53 | |
| CaO | 2.66±0.12 | | 2.13±0.45 | | 2.33±0.30 | | 3.02±0.10 | | 3.28±0.08 | | 4.23±1.36 | | 3.24±0.12 | |
| $Na_2O$ | 0.09±0.02 | | 0.07±0.03 | | 0.08±0.05 | | 0.13±0.03 | | 0.12±0.03 | | 0.44±0.47 | | 0.04±0.01 | |
| $K_2O$ | 0.03±0.02 | | 0.03±0.01 | | 0.03±0.01 | | 0.03±0.02 | | 0.01±0.01 | | 0.23±0.47 | | 0.05±0.02 | |
| LOI | nd | | nd | | nd | | nd | | nd | | nd | | nd | |
| total | 89.74±2.10 | | 90.90±2.18 | | 90.86±1.45 | | 88.98±2.44 | | 90.37±0.91 | | 88.98±2.23 | | 85.70±2.45 | |
| Mg# % | 69 | | 69 | | 67 | | 70 | | 70 | | 65 | | 70 | |
| $Fe^{3+}$% | 64 | | 67 | | 67 | | 90 | | 90 | | 90 | | 93 | |
| $^{IV}Si$ | 6.55±0.09 | | 6.65±0.08 | | 6.65±0.10 | | 6.59±0.04 | | 6.64±0.04 | | 6.66±0.19 | | 6.71±0.04 | |
| $^{IV}Al$ | 1.42±0.09 | | 1.35±0.08 | | 1.35±0.10 | | 1.41±0.04 | | 1.36±0.04 | | 1.34±0.19 | | 1.29±0.04 | |
| $^{IV}Fe^{3+}$ | 0 | | 0 | | 0 | | 0 | | 0 | | 0 | | 0 | |
| $^{VI}Al$ | 0 | | 0 | | 0 | | 0 | | 0 | | 0 | | 0 | |
| $^{VI}Fe^{3+}$ | 1.17±0.05 | | 1.32±0.04 | | 1.85±0.16 | | 1.67±0.00 | | 1.67±0.15 | | 1.87±0.25 | | 1.64±0.08 | |
| $^{VI}Cr$ | 0.00±0.00 | | 0.02±0.00 | | 0.00±0.00 | | 0.00±0.09 | | 0.00±0.00 | | 0.00±0.00 | | 0.00±0.00 | |
| $^{VI}Ti$ | 0.00±0.00 | | 0.00±0.00 | | 0.01±0.02 | | 0.00±0.00 | | 0.01±0.02 | | 0.06±0.08 | | 0.01±0.00 | |
| $^{VI}Fe^{2+}$ | 0.66±0.03 | | 0.57±0.03 | | 0.14±0.01 | | 0.19±0.01 | | 0.19±0.02 | | 0.21±0.03 | | 0.12±0.01 | |
| $^{VI}Ni$ | -- | | -- | | -- | | 0.00±0.00 | | 0.00±0.00 | | 0.00±0.00 | | 0.01±0.00 | |
| $^{VI}Mn$ | 0.01±0.00 | | 0.01±0.00 | | 0.01±0.01 | | 0.07±0.01 | | 0.09±0.01 | | 0.09±0.01 | | 0.01±0.00 | |
| $^{VI}Mg$ | 4.16±0.26 | | 4.12±0.11 | | 3.94±0.26 | | 4.25±0.28 | | 4.35±0.39 | | 3.92±0.65 | | 4.15±0.20 | |
| Σ $^{VI}M$ | 6.00±0.28 | | 6.02±0.14 | | 5.95±0.39 | | 6.18±0.34 | | 6.32±0.35 | | 6.15±0.44 | | 5.94±0.28 | |
| $^{XII}Ca$ | 0.42±0.02 | | 0.33±0.07 | | 0.48±0.05 | | 0.68±0.03 | | 0.74±0.03 | | 0.98±0.33 | | 0.54±0.02 | |
| $^{XII}Na$ | 0.03±0.01 | | 0.02±0.01 | | 0.03±0.03 | | 0.04±0.01 | | 0.03±0.01 | | 0.13±0.14 | | 0.01±0.00 | |
| $^{XII}K$ | 0.01±0.00 | | 0.01±0.00 | | 0.01±0.00 | | 0.01±0.00 | | 0.00±0.00 | | 0.05±0.09 | | 0.01±0.00 | |
| Σ Charge | +0.91±0.67 | | +0.71±0.35 | | +1.17±0.84 | | +2.02±0.82 | | +2.06±0.76 | | +3.11±1.00 | | +1.34±0.67 | |
| Interlayer Charge | +0.88±0.06 | | +0.69±0.15 | | +1.00±0.05 | | +1.41±0.06 | | +1.51±0.06 | | +2.14±0.88 | | +1.10±0.05 | |

**Table 3 (Continued).** Chemical Compositions (EMP) and Structural Formulae of Saponites from Griffith Park, CA, and Others.

| Sample | CAS | CAS | CAS | L&S | Vicente | Vicente | Komadel | Cloutis | Chukanov |
|---|---|---|---|---|---|---|---|---|---|
| Type | Vf-c 1σ | ExOl 1σ | Meso 1σ | 1917 | 1996 | 1998* | 2000* | 2014 | 2003 |
| $SiO_2$ | 43.53±2.5 | 45.87±1.56 | 44.92±1.94 | 39.64 | 54.03 | 48.07 | 55.82 | 47.63 | 33.15 |
| $TiO_2$ | 0.02±0.02 | 0.17±0.04 | 0.18±0.10 | 0.00 | 0.38 | 0.65 | 0.53 | 0.30 | - |
| $Al_2O_3$ | 6.78±0.43 | 7.41±0.36 | 6.62±0.68 | 9.05 | 9.02 | 10.09 | 11.95 | 10.01 | 9.95 |
| $Cr_2O_3$ | 0.02±0.02 | 0.02±0.02 | 0.08±0.12 | - | - | - | - | - | - |
| $FeO_T$ | 13.86±0.19 | 13.42±0.72 | 15.98±1.48 | 14.42 | 14.77 | 16.87 | 13.52 | 17.02 | 29.13 |
| NiO | 0.07±0.02 | 0.09±0.02 | 0.06±0.02 | - | - | - | - | - | - |
| MnO | 0.05±0.04 | 0.06±0.04 | 0.07±0.04 | - | .59 | 0.33 | 0.55 | 0.40 | - |
| MgO | 17.92±1.48 | 18.88±0.54 | 16.21±1.00 | 15.80 | 15.28 | 16.41 | 14.09 | 17.79 | 6.62 |
| CaO | 3.07±0.12 | 3.32±0.09 | 3.59±0.27 | 2.93 | 4.52 | 4.71 | 2.48 | 4.36 | 3.31 |
| $Na_2O$ | 0.05±0.02 | 0.04±0.01 | 0.12±0.13 | 0.71 | 0.86 | 1.16 | - | 0.74 | 0.21 |
| $K_2O$ | 0.05±0.02 | 0.05±0.02 | 0.04±0.02 | 0.00 | 0.11 | 0.12 | 0.16 | 0.07 | 0.07 |
| LOI | nd | nd | nd | 17.21 | 17.09 | nd | nd | 17.25 | nd |
| total | 85.42±2.62 | 89.29±1.80 | 87.87±1.88 | 99.76 | 99.52 | *98.14 | *99.11 | 98.31 | 82.44 |
| Mg# % | 70 | 71 | 65 | 66 | 64 | 63 | 65 | 65 | 29 |
| $Fe^{3+}$% | 92 | 93 | 93 | 46 | 87 | 87 | 87 | 76 | 27 |
| $^{IV}Si$ | 6.76±0.03 | 6.72±0.05 | 6.82±0.09 | 6.30 | 6.68 | 6.41 | 6.39 | 6.41 | 5.82 |
| $^{IV}Al$ | 1.24±0.03 | 1.28±0.05 | 1.18±0.09 | 1.70 | 1.32 | 1.59 | 1.61 | 1.59 | 2.06 |
| $^{IV}Fe^{3+}$ | 0 | 0 | 0 | 0 | 0 | 0 | 0 | - | 0.12 |
| $^{VI}Al$ | 0 | 0 | 0 | 0 | 0 | 0 | 0 | 0 | 0 |
| $^{VI}Fe^{3+}$ | 1.67±0.10 | 1.53±0.11 | 1.89±0.05 | 0.88 | 1.33 | 1.64 | 1.13 | 1.46 | 1.04 |
| $^{VI}Cr$ | 0.00±0.00 | 0.00±0.00 | 0.01±0.01 | - | 0.00 | 0.00 | 0.00 | - | - |
| $^{VI}Ti$ | 0.00±0.00 | 0.02±0.01 | 0.02±0.01 | 0.00 | 0.03 | 0.07 | 0.05 | 0.03 | - |
| $^{VI}Fe^{2+}$ | 0.13±0.01 | 0.12±0.01 | 0.14±0.02 | 1.04 | 0.20 | 0.25 | 0.17 | 0.46 | 3.12 |
| $^{VI}Ni$ | 0.01±0.00 | 0.01±0.00 | 0.01±0.00 | - | - | - | - | - | - |
| $^{VI}Mn$ | 0.01±0.00 | 0.01±0.00 | 0.01±0.00 | - | 0.06 | 0.04 | 0.05 | 0.05 | - |
| $^{VI}Mg$ | 4.15±0.50 | 4.11±0.15 | 3.67±0.30 | 3.75 | 2.82 | 3.21 | 2.41 | 3.57 | 1.74 |
| $\Sigma\ ^{VI}M$ | 5.97±0.58 | 5.80±0.21 | 5.74±0.47 | 5.66 | 4.44 | 5.20 | 3.80 | 5.57 | 2.95 |
| $^{XII}Ca$ | 0.51±0.03 | 0.52±0.02 | 0.81±0.09 | 0.50 | 0.60 | 0.67 | 0.31 | 0.88 | 0.61 |
| $^{XII}Na$ | 0.02±0.01 | 0.01±0.01 | 0.03±0.04 | 0.22 | 0.21 | 0.30 | - | 0.19 | 0.08 |
| $^{XII}K$ | 0.01±0.00 | 0.01±0.00 | 0.01±0.00 | 0.00 | 0.02 | 0.02 | 0.02 | 0.01 | 0.02 |
| Σ Charge | +1.83±1.29 | +0.95±0.52 | +1.44±1.30 | -0.27 | -1.62 | +0.24 | -4.17 | +0.11 | +0.57 |
| Interlayer Charge | +1.05±0.07 | +1.06±0.06 | +1.66±0.22 | +1.22 | +1.43 | +1.84 | +0.64 | +1.96 | +1.32 |

Samples: AMNH – AMNH89172; MU, from Minerals Unlimited; CAS – from California Academy of Sciences. Types. ExOl – replacement of olivine phenocrysts. Vf-c – coarse-grained vesicle fill. Vf-f – fine-grained vesicle fill. Normalization to 44 total cation charges, to balance $O_{20}(OH)_4$. Roman numeral superscripts are site coordinations. Fe redox from Mössbauer spectroscopy for AMNH, CAS, and MU; from from wet chemistry and total Fe recalculated as $FeO_T$ for L&S 1917, Vicente 1996 and 1998, Komadel 2000, Chukanov et al. 2003, and Cloutis 2014. * indicates analysis is of dehydrated sample. Uncertainties are from analytical precision, which are significantly larger than uncertainties on accuracy (from analyses of standards).

**Table 4.** Mössbauer Parameters (Room Temperature) for Griffith Saponite Samples.

| | $Fe^{3+}$ Doublet | | | | $Fe^{2+}$ Doublet | | | | Sextet | | | | | |
|---|---|---|---|---|---|---|---|---|---|---|---|---|---|---|
| Sample and Subspectrum | CS mm/s | QS mm/s | FWHM mm/s | A % | CS mm/s | QS mm/s | FWHM mm/s | A % | CS mm/s | QS mm/s | $B_{hf}$, T | A % | $Fe^{3+}/\Sigma Fe$ | Assignment |
| AMNH89172_PHY, Coarse-grained dark globule separate | | | | | | | | | | | | | 0.64 | |
| Doublet 3D1 | 0.36 | 1.35 | 0.47 | 46 | --- | --- | --- | --- | --- | --- | --- | --- | --- | Saponite |
| Doublet 3D2 | 0.39 | 0.83 | 0.40 | 18 | --- | --- | --- | --- | --- | --- | --- | --- | --- | Saponite |
| Doublet 2D1 | --- | --- | --- | --- | 1.14 | 2.62 | 0.34 | 36 | --- | --- | --- | --- | --- | Saponite |
| AMNH89172_BAS, Basalt separate | | | | | | | | | | | | | 0.50 | |
| Doublet 3D1 | 0.36 | 1.33 | 0.51 | 15 | --- | --- | --- | --- | --- | --- | --- | --- | --- | Saponite |
| Doublet 3D2 | 0.38 | 0.71 | 0.60 | 16 | --- | --- | --- | --- | --- | --- | --- | --- | --- | Saponite |
| Doublet 2D1 | --- | --- | --- | --- | 1.14 | 2.63 | 0.33 | 17 | --- | --- | --- | --- | --- | Saponite |
| Doublet 2D2 | --- | --- | --- | --- | 1.14 | 2.02 | 0.47 | 32 | --- | --- | --- | --- | --- | Pyroxene? |
| Sextet S1 | --- | --- | --- | --- | --- | --- | --- | --- | 0.37 | -0.21 | 51.0 | 11 | --- | Hematite |
| Sextet S2A | --- | --- | --- | --- | --- | --- | --- | --- | [0.26] | [-0.02] | [49.0] | 6 | --- | Magnetite (tet) |
| Sextet S2B | --- | --- | --- | --- | --- | --- | --- | --- | [0.67] | [0.00] | [46.0] | 5 | --- | Magnetite (oct) |
| MUGPLA1_PHY, Coarse grained dark globule separate | | | | | | | | | | | | | 0.85 | |
| Doublet 3D1 | 0.38 | 1.38 | 0.54 | 54 | --- | --- | --- | --- | --- | --- | --- | --- | --- | Saponite |
| Doublet 3D2 | 0.35 | 0.83 | 0.47 | 30 | --- | --- | --- | --- | --- | --- | --- | --- | --- | Saponite |
| Doublet 2D1 | --- | --- | --- | --- | [1.14] | 2.61 | 0.36 | 15 | --- | --- | --- | --- | --- | Saponite |
| CASGP1-F, Fine-grained brown vein separate | | | | | | | | | | | | | 0.93 | |
| Doublet 3D1 | 0.38 | 1.31 | 0.45 | 31 | --- | --- | --- | --- | --- | --- | --- | --- | --- | Saponite |
| Doublet 3D2 | 0.36 | 0.78 | 0.45 | 35 | --- | --- | --- | --- | --- | --- | --- | --- | --- | Saponite |
| Doublet 3D3 | 0.31 | 0.39 | 0.45 | 24 | --- | --- | --- | --- | --- | --- | --- | --- | --- | npOx |
| Doublet 2D1 | --- | --- | --- | --- | [1.14] | 2.55 | 0.31 | 7 | --- | --- | --- | --- | --- | Saponite |
| Sextet S1 | --- | --- | --- | --- | --- | --- | --- | --- | 0.38 | -0.20 | 51.1 | 3 | --- | Hematite |
| CASGP1-C, Coarse-grained dark globule separate | | | | | | | | | | | | | 0.92 | |
| Doublet 3D1 | 0.36 | 1.34 | 0.44 | 31 | --- | --- | --- | --- | --- | --- | --- | --- | --- | Saponite |
| Doublet 3D2 | 0.36 | 0.86 | 0.44 | 35 | --- | --- | --- | --- | --- | --- | --- | --- | --- | Saponite |
| Doublet 3D3 | 0.32 | 0.46 | 0.44 | 26 | --- | --- | --- | --- | --- | --- | --- | --- | --- | npOx |
| Doublet 2D1 | --- | --- | --- | --- | [1.14] | 2.67 | 0.30 | 8 | --- | --- | --- | --- | --- | Saponite |

Mössbauer parameters are center shift (CS, with respect to metallic Fe foil at room temperature, quadrupole splitting (QS), magnetic hyperfine field strength ($B_{hf}$), and subspectral area (A; f-factor corrected). Uncertainty for CS, QS, and FWHM is ±0.02 mm/s. Uncertainty for A is ±2 % (absolute). FWHM of doublets 3D1, 3D2, and 3D3 constrained equal during the fitting procedure for CASGP1-C and CASGP1-F. CS for doublet 2D1 constrained to 1.14 mm/s during the fitting procedure for MUGPLA1, CASGP1-C, and CASGP1-F. Samples AMNH89172_PHY, MUGPLA1_PHY, CASGP1-F, and CASGP1-C correspond to AMNH Vf-c and ExOl combined, MU Vf-c and ExOl combined, CAS Vf-f, and CAS Vf-c, respectively in Table 3.

**Table 5**. Selected Mössbauer, XRD, and VNIR Data for Griffith Saponite Samples Measured Under Different Environmental Conditions.

| | | XRD | | | VNIR Spectral Region | | | | |
|---|---|---|---|---|---|---|---|---|---|
| Sample | $Fe^{3+}/\square Fe$ | 001 (Å) | 005 (Å) | 02l (Å) | OH (μm) | HOH (μm) | MOH (μm) | MOH (μm) | Environmental Condition |
| AMNH89172_PHY | 0.64 | 14.7 | 2.96 | 4.59 | 1.410 | 1.909 | 2.316 | 2.401 | Equilibrated in lab air |
| AMNH89172_PHY | --- | 11.9 | --- | 4.59 | --- | --- | --- | --- | Equilibrated in dry $N_2$ in CheMin-IV |
| AMNH89172_PHY | --- | 15.0 | 3.01 | 4.59 | --- | --- | --- | --- | Re-equilibrated in lab air 72 hr after dry $N_2$ exposure |
| AMNH89172_PHY | --- | --- | --- | --- | 1.405 | 1.911 | 2.315 | 2.403 | Equilibrated in dry $N_2$ for 436 hr (no air exposure) |
| AMNH89172_PHY | --- | --- | --- | --- | 1.405 | 1.911 | 2.315 | 2.401 | Equilibrated in dry $N_2$ at 110 C for 1152 hr (no air exposure) |
| AMNH89172_PHY | --- | --- | --- | --- | 1.405 | 1.911 | 2.315 | 2.400 | Equilibrated in dry $N_2$ at 220 C for 216 hr (no air exposure) |
| AMNH89172_PHY | | 15.0 | 3.01 | 4.59 | 1.413 | 1.912 | 2.315 | 2.400 | Re-equilibrated in lab air 16 hr after heating in dry $N_2$ |
| MUGPLA1_PHY | 0.85 | 15.0 | 3.01 | 4.59 | 1.414 | 1.912 | 2.308 | 2.400 | Equilibrated in lab air |
| CASGP1-F | 0.89 | 15.0 | 3.02 | 4.59 | 1.415 | 1.912 | 2.300 | 2.395 | Equilibrated in lab air |
| CASGP1-C | 0.90 | 15.0 | 3.02 | 4.59 | 1.415 | 1.912 | 2.301 | 2.396 | Equilibrated in lab air |
| CASGP1-C | --- | 11.8 | --- | 4.58 | --- | --- | --- | --- | Equilibrated in dry $N_2$ in CheMin-IV |
| Uncertainty | 0.02 | 0.01 | 0.01 | 0.01 | 0.002 | 0.002 | 0.002 | 0.002 | |

All measurements made on CheMin-IV transmission XRD at room temperature, corrected for Lorentz polarization. --- = not determined.

Figure 1.

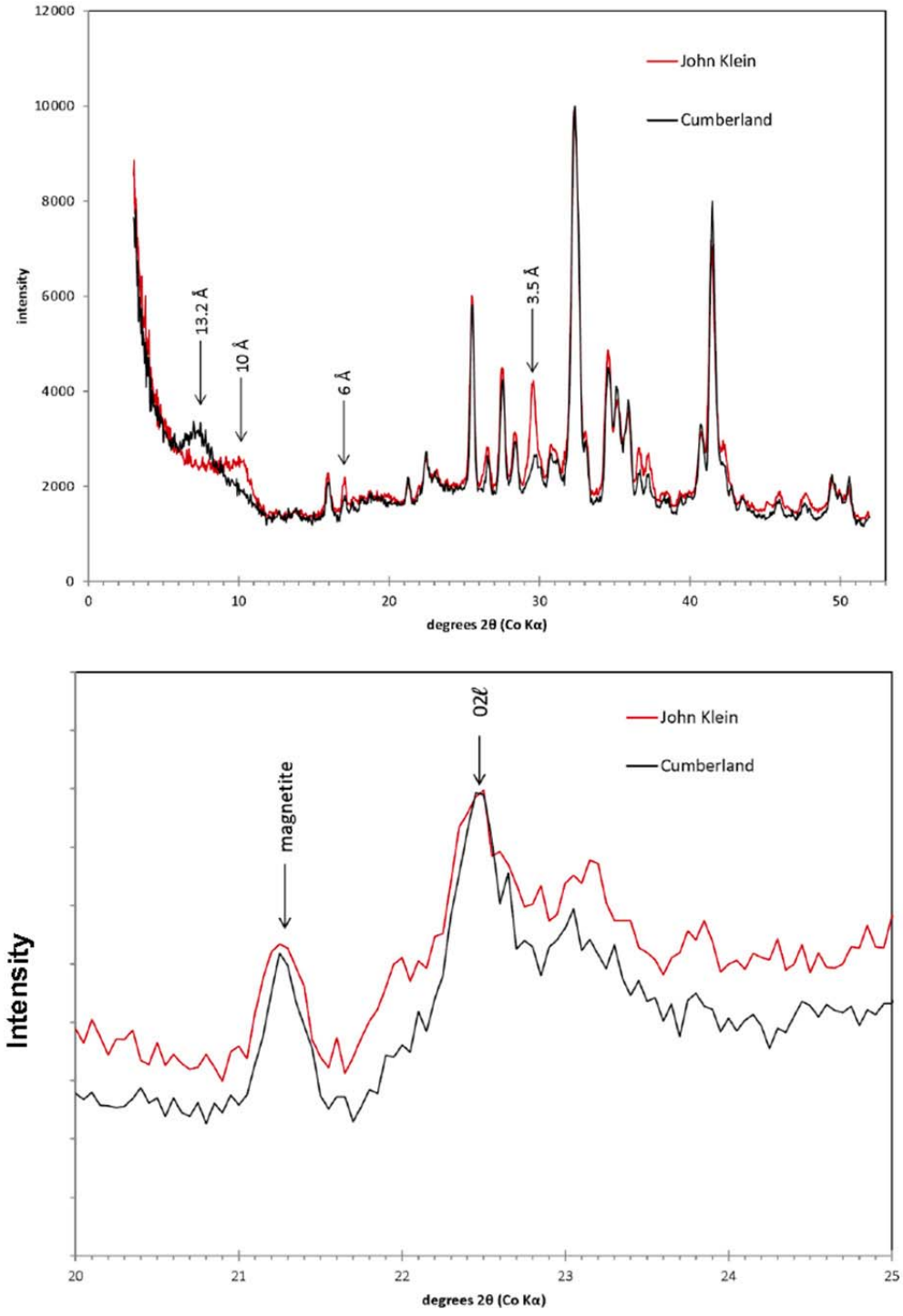

Figure 2

Fig 2a

Fig 2b


Fig 2c

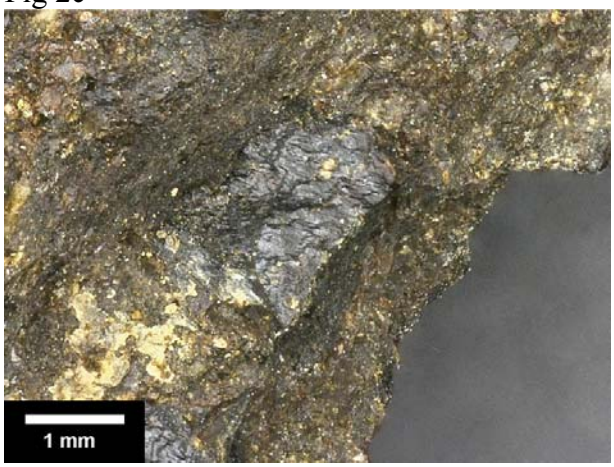


Fig 2d

Fig 2e

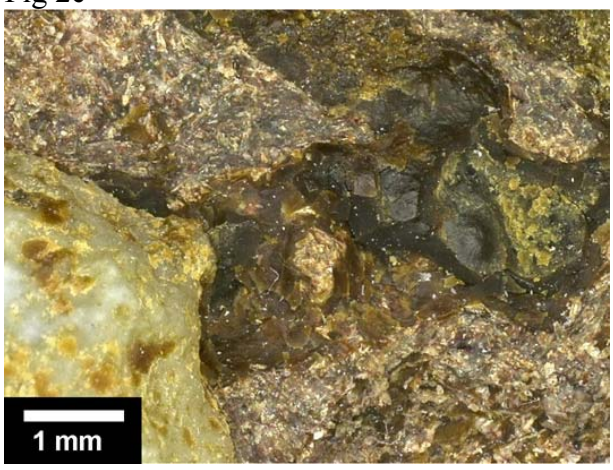

Figure 3.

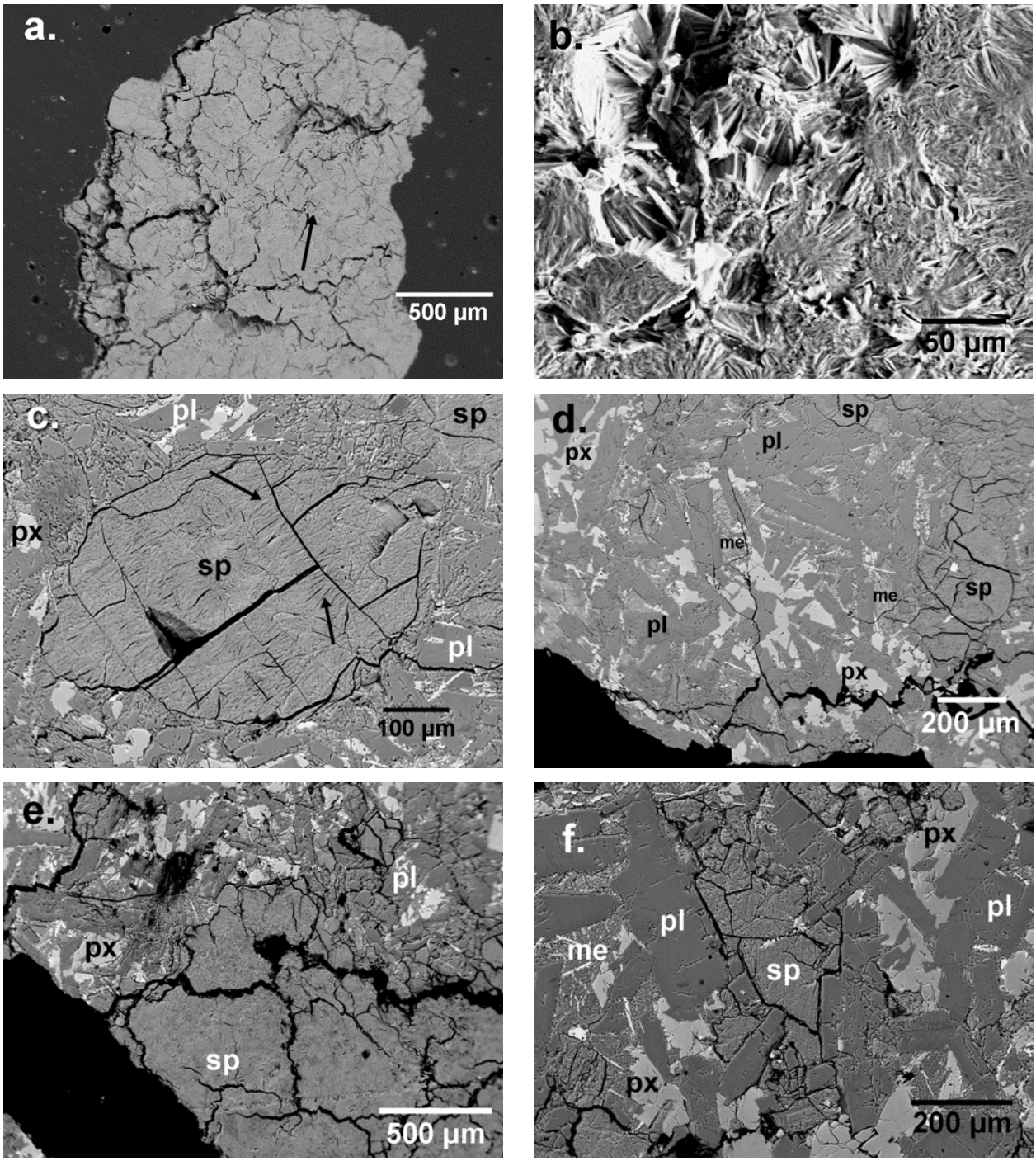

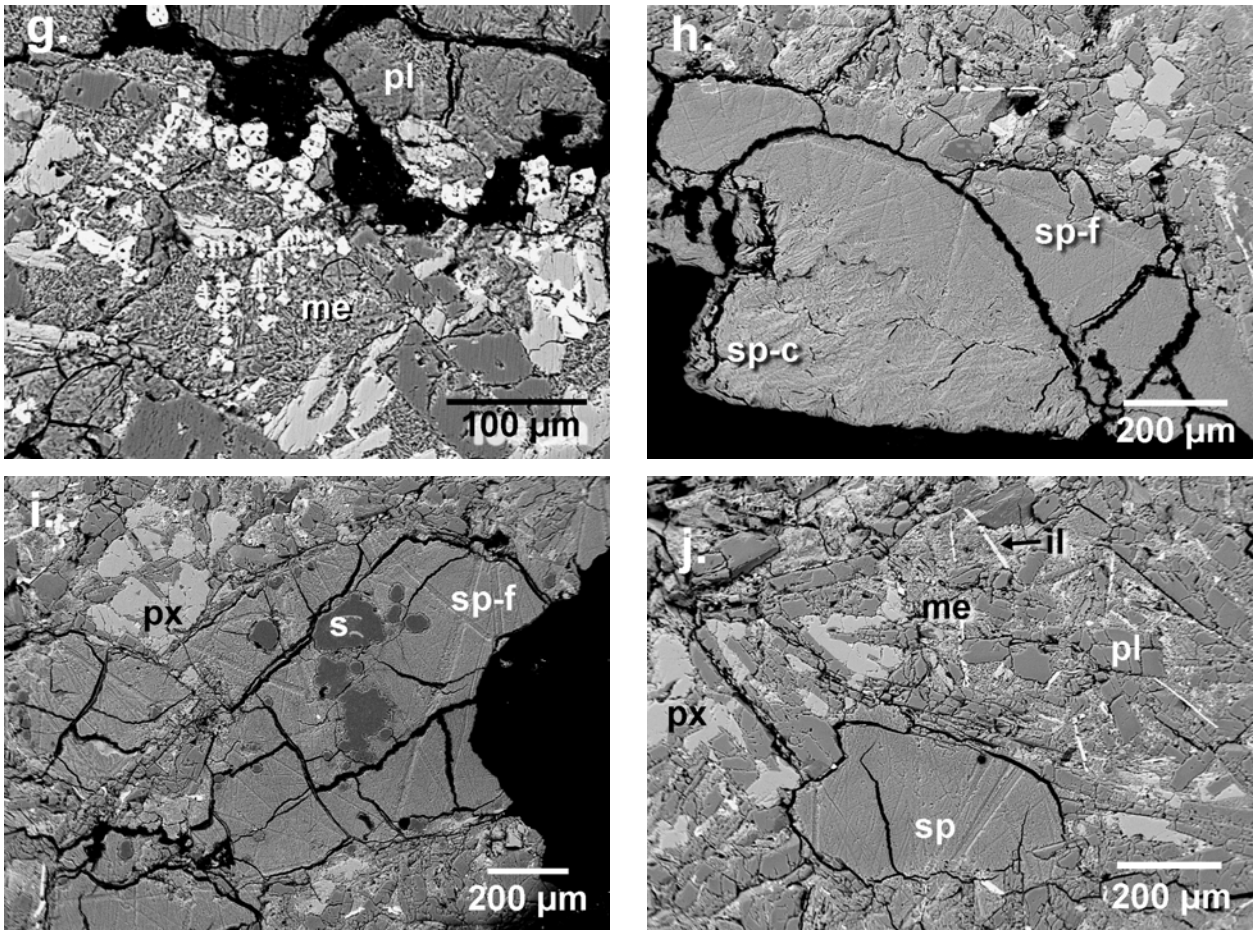

Figure 4

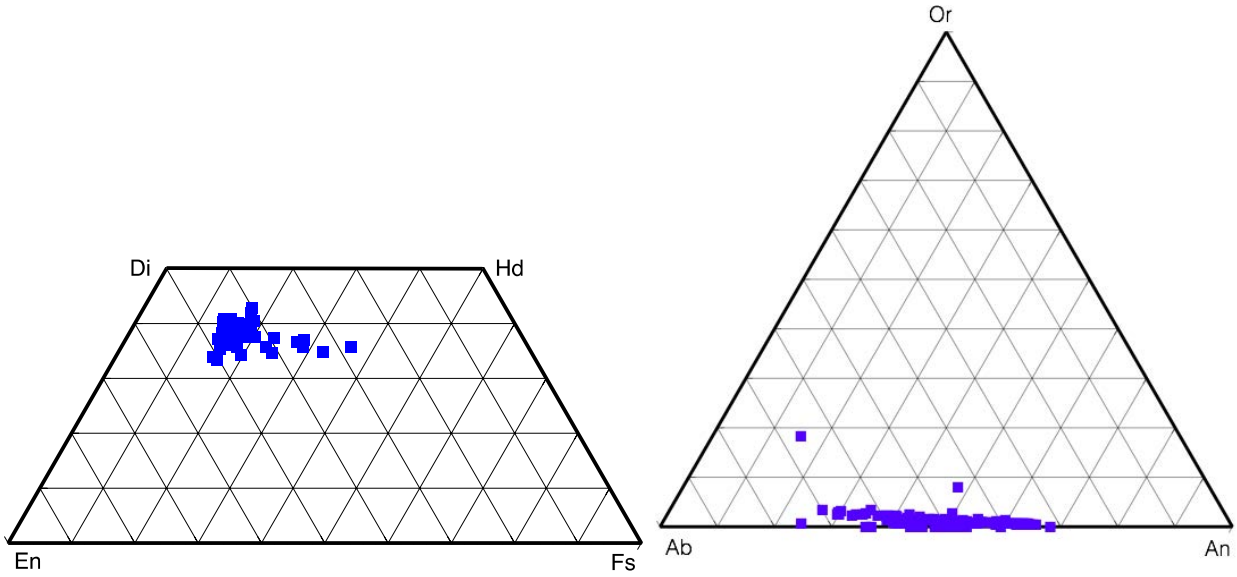

Figure 5

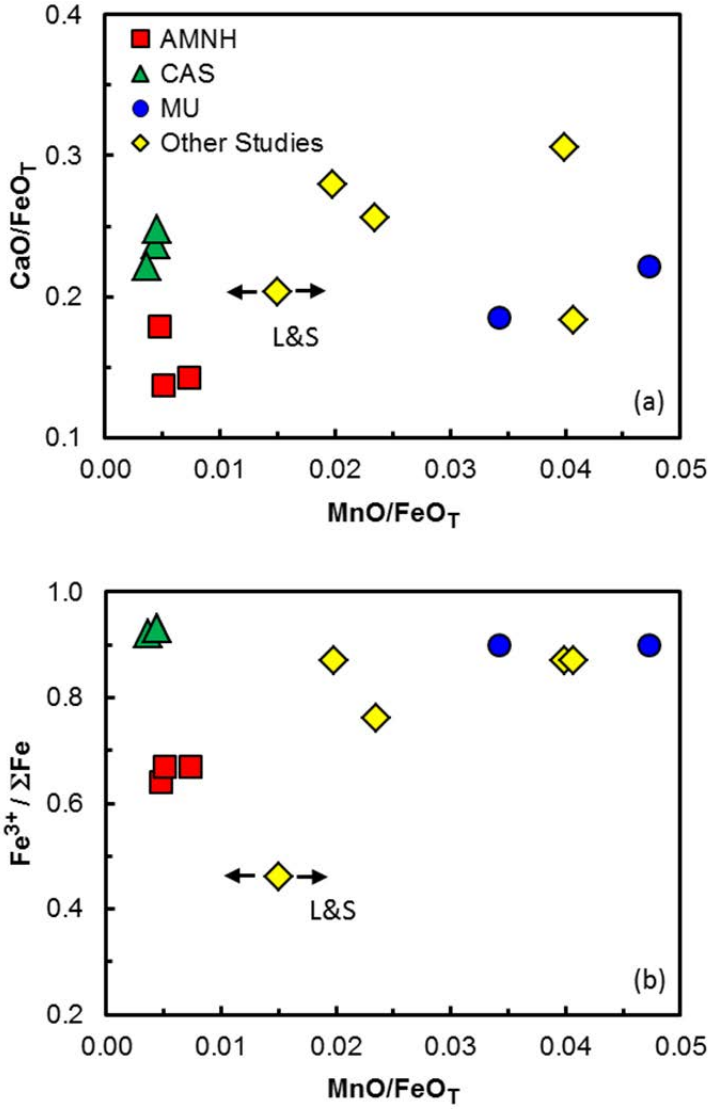

Figure 6.

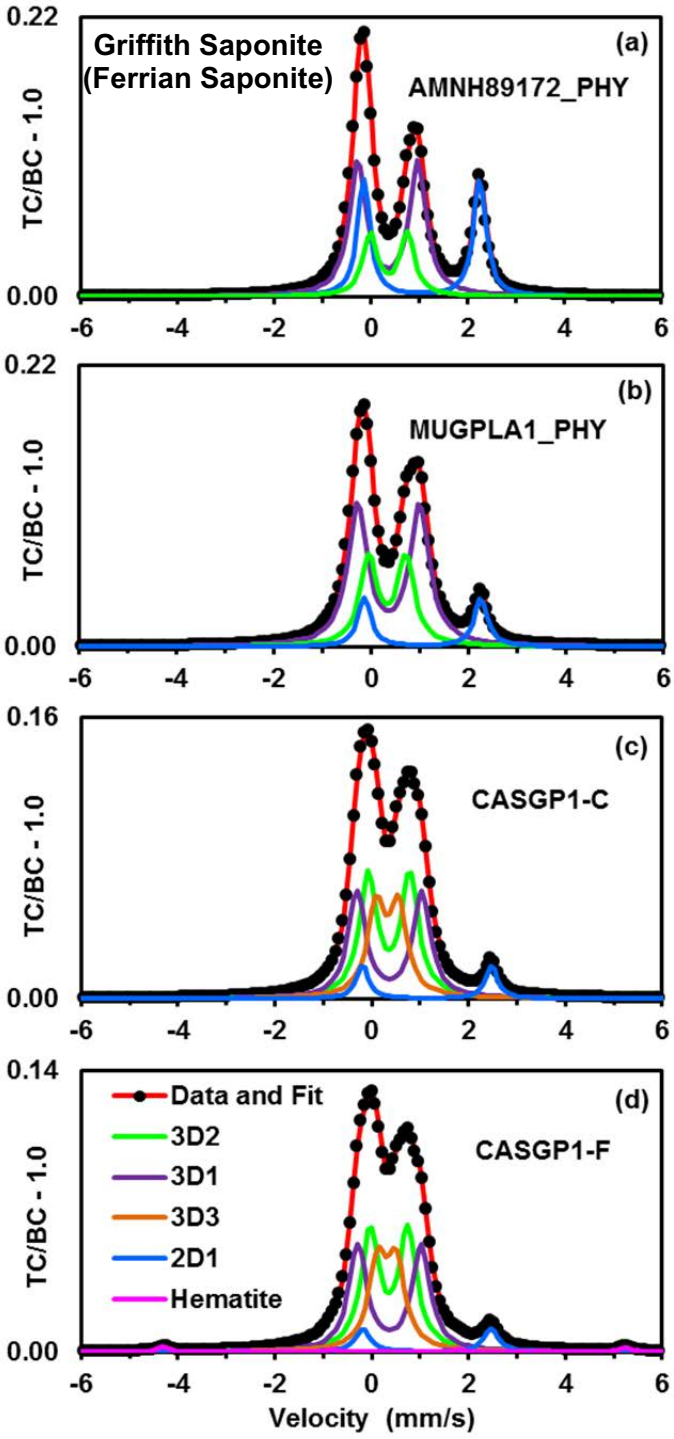

Figure 7.

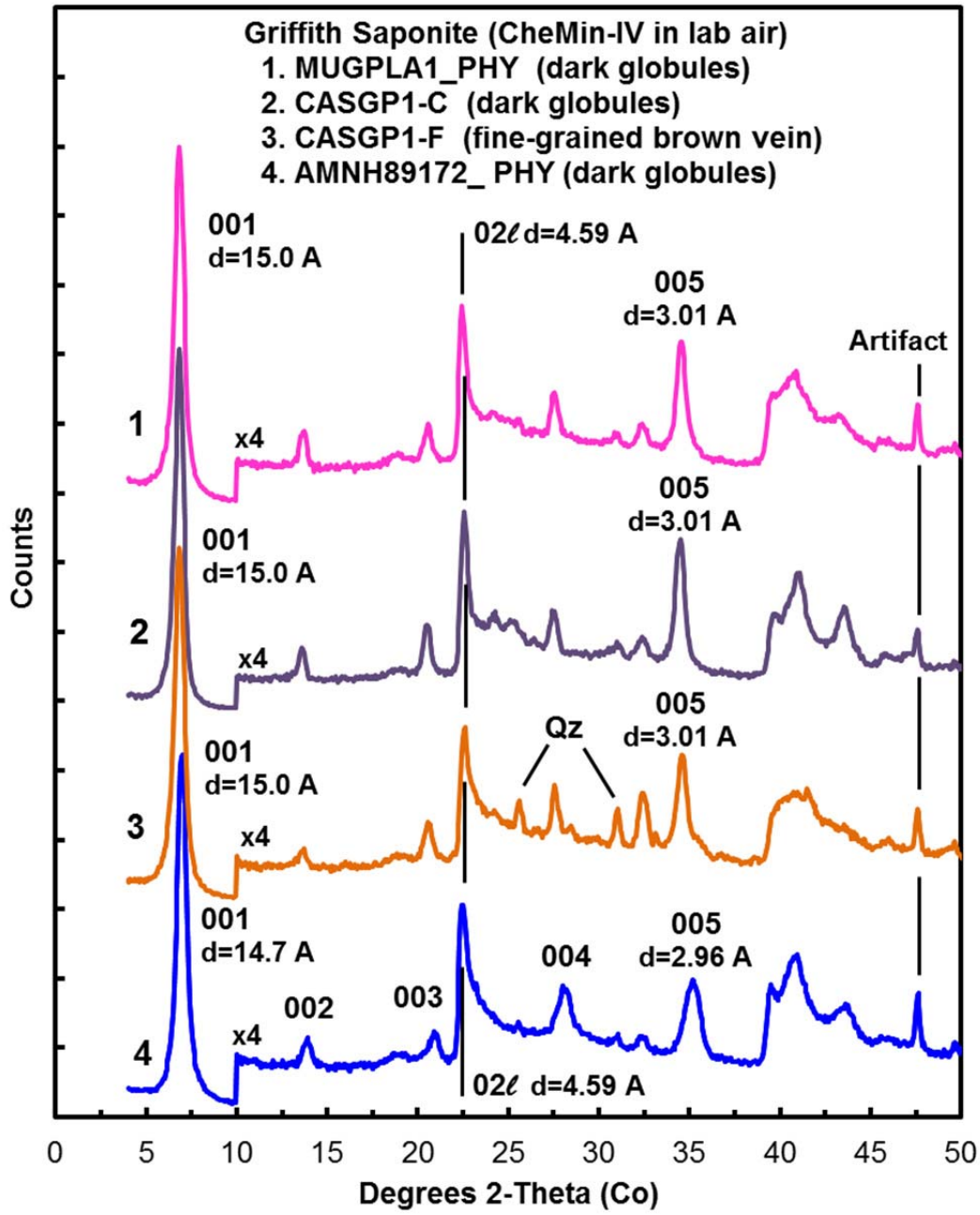

Figure 8.

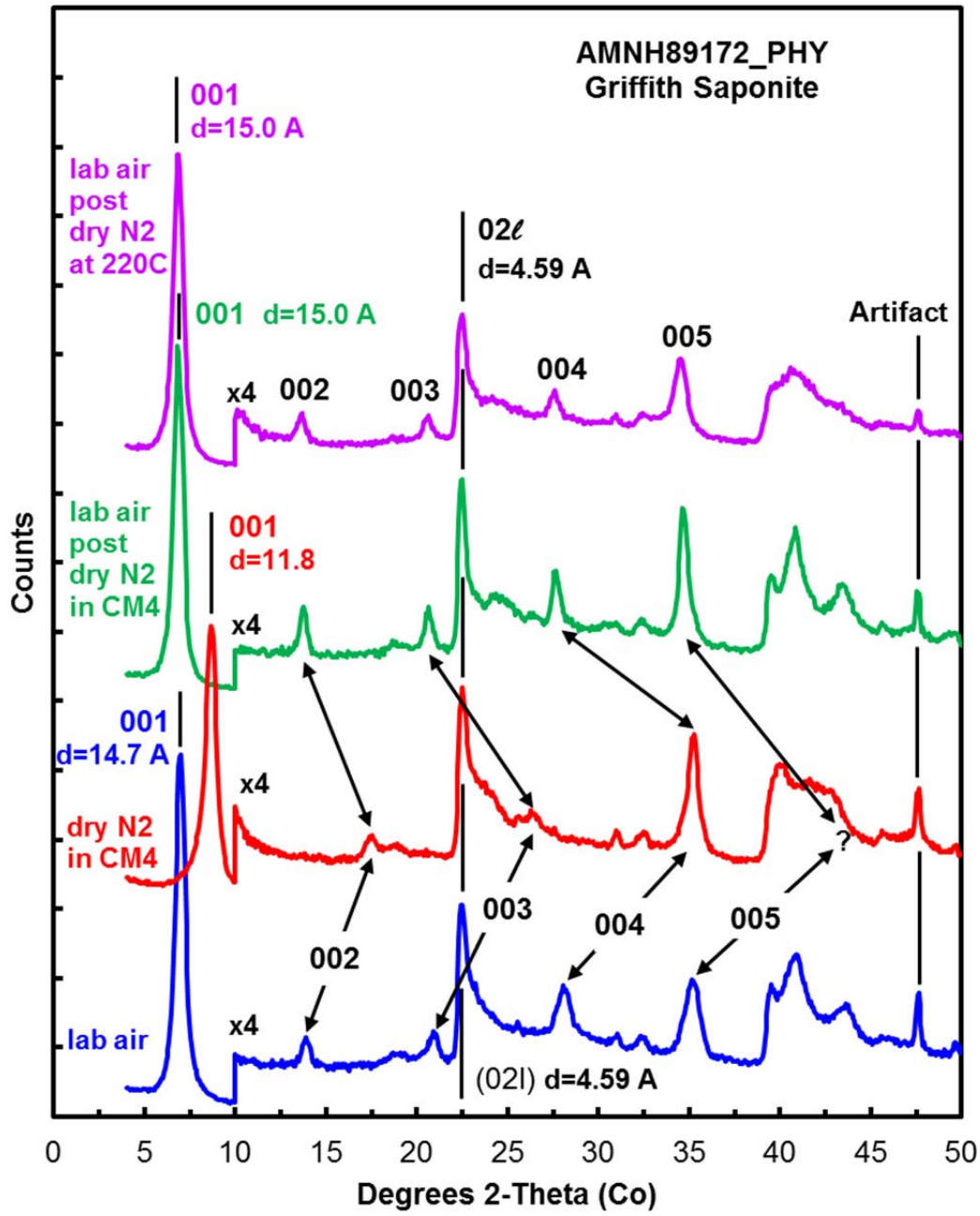

Figure 9.

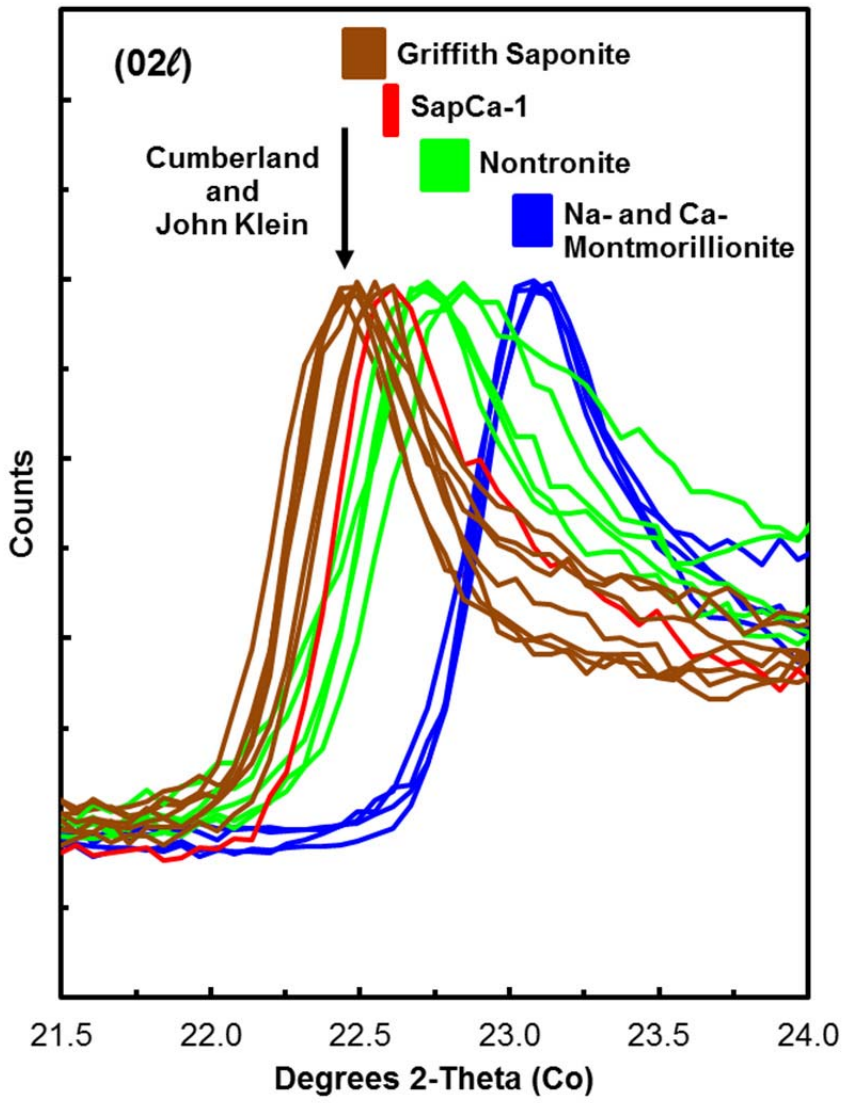

Figure 10

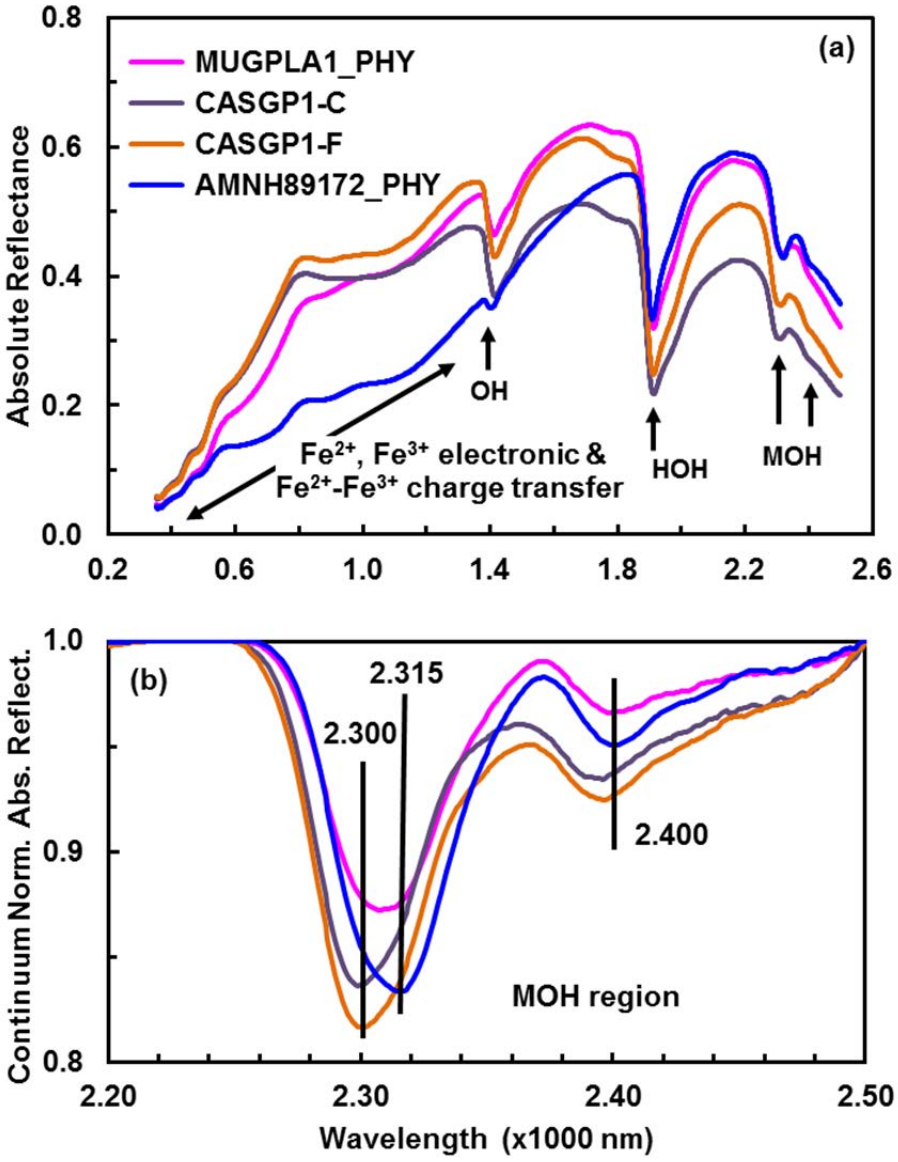

Figure 11.